Experimental and Theoretical Study of Aqueous *cis*-Pinonic Acid Photolysis

Hanna Lignell,[†,‡] Scott A. Epstein,[†] Margaret R. Marvin,[†] Dorit Shemesh,[§] Benny Gerber,[†,‡,§] and Sergey Nizkorodov*,[†]

[†]Department of Chemistry, University of California, Irvine, California 92697-2025, United States
[‡]Laboratory of Physical Chemistry, University of Helsinki, P.O. Box 55, FIN-00014 Helsinki, Finland
[§]Institute of Chemistry and The Fritz Haber Research Center, The Hebrew University, Jerusalem 91904, Israel

Ⓢ *Supporting Information*

ABSTRACT: Direct aqueous photolysis of *cis*-pinonic acid (PA; 2-(3-acetyl-2,2-dimethylcyclobutyl)acetic acid; CAS Registry No. 473-72-3) by 280−400 nm radiation was investigated. The photolysis resulted in Norrish type II isomerization of PA leading to 3-isopropenyl-6-oxoheptanoic acid (CAS Registry No. 4436-82-2), also known as limononic acid, as the major product, confirmed by ^{1}H and ^{13}C NMR analysis, chemical ionization mass spectrometry, and electrospray ionization mass spectrometry. Several minor products resulting from Norrish type I splitting of PA were also detected. The molar extinction coefficients of aqueous PA were measured and used to calculate the photolysis quantum yield of aqueous PA as 0.5 ± 0.3 (effective average value over the 280−400 nm range). The gas-phase photolysis quantum yield of 0.53 ± 0.06 for PA methyl ester (PAMe; CAS Registry No. 16978-11-3) was also measured for comparison. These results indicate that photolysis of PA is not significantly suppressed by the presence of water. This fact was confirmed by photodissociation dynamics simulations of bare PA and of PAMe hydrated with one or five water molecules using on-the-fly dynamics simulations on a semiempirical potential energy surface. The calculations correctly predicted the occurrence of both Norrish type I and Norrish type II photolysis pathways, both driven by the dynamics on the lowest triplet excited state of PA and PAMe. The rate of removal of PA by direct aqueous photolysis in cloudwater and in aerosol water was calculated for a range of solar zenith angles and compared with rates of other removal processes such as gas-phase oxidation by OH, aqueous-phase oxidation by OH, and gas-phase photolysis. Although the direct photolysis mechanism was not the most significant sink for PA in cloud and fog droplets, direct photolysis can be expected to contribute to removal of PA and more soluble/less volatile biogenic oxidation products in wet particulate matter.
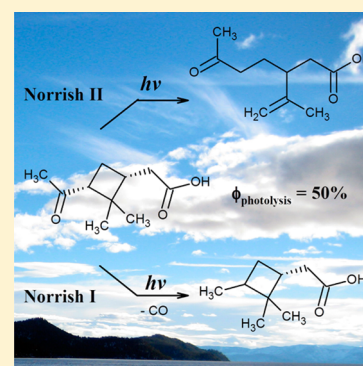
I. INTRODUCTION

Atmospheric aerosols play a critical role in controlling climate, driving chemical reactions in the atmosphere, acting as surfaces for heterogeneous reactions, and contributing to air pollution problems and indoor air quality issues worldwide.[1,2] Oxidation of biogenic volatile organic compounds (BVOC) such as isoprene and α-pinene serves as the dominant source of secondary organic aerosols (SOA). The global α-pinene emissions estimated at 66 Tg/yr are larger than emissions of any other BVOC with the exception of methanol and isoprene.[3] Once emitted, α-pinene is quickly oxidized by O$_3$, OH, and NO$_3$, leading to the production of *cis*-pinonic acid, pinic acid, and pinonaldehyde as major products, as well as a variety of other multifunctional organic compounds (carboxylic acids, ketones, aldehydes, alcohols, peroxides, and sulfur- and nitrogen-containing species), which partition into SOA particles and water droplets. A large number of studies focusing on the chemical mechanism of α-pinene oxidation have appeared in the literature over the years; the reader is referred to ref 4 for a list of representative studies.

cis-Pinonic acid, subsequently abbreviated as PA, is one of the major products of α-pinene oxidation and an important tracer of α-pinene chemistry. It possesses a carbonyl and a carboxyl group, as do many other multifunctional products of BVOC oxidation. The presence of the carbonyl group makes PA photolyzable (the carboxyl group of PA is not expected to directly participate in photolysis).[1] It is moderately soluble in water, with a Henry's law constant of 2×10^7 M/atm predicted from HENRYWIN v3.20,[5] and has intermediate volatility, with a saturation mass concentration of C* = 5.2 μg/m^3.[6] Therefore, it can exist in the gas phase, in particles, and in the aqueous phase. PA has been observed in several laboratory studies of SOA production from terpene oxidation,[7−10] and a study concerning the OH-initiated oxidation of PA was recently published.[11] PA has also been detected in fine aerosols found in forested, urban, and rural areas[12,13] and in fog droplets in the

form of PA methyl ester (methyl pinonate).[14] The result of the study of O'Dowd et al. indicated that aerosol formation in clouds over forests is driven by condensable organic vapors, including PA.[15] Both experimental and computational results show that PA efficiently lowers the surface tension of water clusters, thus playing an important role in the availability of atmospheric aerosol particles for cloud formation.[16,17]

Aqueous environments (cloud/fogwater, aerosol water, and ice) play a significant role in the photochemical processing of water-soluble organic compounds (WSOC). Even though atmospheric liquid water content is relatively low (typically <0.5 g liquid per cubic meter of air), water droplets and ice crystals provide unique conditions for aqueous-phase photo-chemistry of WSOC.[18−21] WSOC may remain dissolved in cloud and fog droplets for significant periods of time, and the aqueous-phase chemistry taking place in these conditions can be quite different from reactions in the gas phase or in dry SOA particles. Aerosol water carries even less mass and is typically saturated with dissolved inorganic salts and WSOC (it has been estimated that aerosol water exceeds dry aerosol mass by a factor of 2−3),[22,23] but it can also sustain unique photo-chemistry. Oxidation products of BVOC can access aqueous aerosol particles via wet deposition and undergo oxidation processes in the aqueous phase.[24−29] The aqueous phase can offer new uptake mechanisms, change the oxidation state of organics compared to dry particles,[30] and lead to formation of unique products that do not have efficient gas-phase sources.[31] It is believed that aqueous SOA chemistry could explain the discrepancies between the chemical properties predicted from gas-phase oxidation mechanisms and the chemical properties of SOA measured in the field.[32−37] However, the reaction mechanisms and potential organic precursors of aqueous SOA photochemistry are not well understood.

This work focuses on aqueous and gas-phase photolysis of PA as a prototypical carbonyl compound, which bears structural elements similar to those of many other compounds formed by atmospheric oxidation of monoterpenes. PA is a convenient model system because it is semivolatile and water-soluble, making it possible to investigate its photochemistry both in the condensed phase and in the gas phase. To the best of our knowledge, there are no data available related to direct aqueous or gas-phase photolysis of PA, but several groups have studied the photochemistry of structurally similar gas-phase species including cyclobutyl methyl ketone.[38−40] Cycobutyl methyl ketone possesses a substructure similar to PA, providing a model compound for atmospherically related chemistry. Praplan et al. used cyclobutyl methyl ketone as a model compound for PA to study the SOA oxidation mechanisms in the gas phase.[41] Shaffer et al. reported the mechanism of Norrish-II isomerization of nopinone and its photolysis products,[42] offering important clues about the possible mechanism of aqueous photolysis of PA. Gas-phase OH oxidation of PA was shown to produce 3-methyl-1,2,3-butanetricarboxylic acid.[11] Photolysis and OH oxidation of pinonaldehyde have also been studied previously.[10,43] We want to point out that PA will not be representative of two important keto-carboxylic acids, pyruvic acid and glyoxylic acid, which have carbonyl and carboxyl groups on the connected carbon atoms resulting in unique photochemical pathways.[44−46]

This study had several intersecting goals. The most important objective was to provide data needed to quantitatively compare rates for removal of oxidation products of BVOC by direct photolysis and by OH oxidation in both the gas and aqueous phases. To achieve this goal, we picked PA as a prototypical BVOC oxidation product and determined its photolysis quantum yields, major products photolysis, and absorption cross sections. The second objective was to evaluate the usefulness of on-the-fly dynamics simulations on semi-empirical potential energy surfaces for predicting the outcome of photolysis of PA and similar biogenic carbonyls. An extensive set of simulations of photolysis of PA in the gas phase and in small water clusters was carried out to achieve this goal. The third objective was to identify possible tracers specific to direct photolysis processes. Because of the large variety of different chemical processes taking place in the atmosphere in multiple phases, specific tracers of chemistry are exceedingly useful for constraining the possible chemical mechanisms. Although the specific tracer (3-methyl-1,2,3-butanetricarboxylic acid)[11] for gas-phase OH oxidation of PA has been identified, no tracers for photolysis of PA or related compounds are currently known. To achieve this goal, the products of aqueous-phase photolysis of PA were identified and compared to products formed by other reaction pathways. We trust that the comprehensive approach to the mechanism of photolysis of PA will be useful for understanding photochemical fates of other water-soluble biogenic carbonyls.

II. EXPERIMENTAL METHODS

A. Photolysis and Quantum Yield Determination. UV−vis spectroscopy provides means for investigating the photolysis of PA by following the decay of the characteristic π^* ← n carbonyl band as a function of time. By determining the photolysis rate of PA and that of a chemical actinometer under identical experimental conditions, it is possible to quantify the photolysis quantum yield as discussed in detail below and in the Supporting Information. PA (Sigma-Aldrich, 98%) was dissolved in HPLC grade water (Fisher Scientific, Omnisolv, HPLC grade) to prepare an 18 mM solution. The sample was then photolyzed in a standard 1 cm cuvette in 15 min time intervals for the first 1 h, and 30 min time intervals up to 3 h. A diagram of the photolysis setup is shown in Figure S1 of the Supporting Information. The cuvette was exposed to room air during photolysis, making it accessible to oxygen. Radiation from a 150 W xenon UV lamp in an air-cooled housing (Newport model 66902) was reflected by a 90° dichroic mirror (Newport model 60159) and filtered with a U-330 band-pass filter (Edmund optics #46-438, center wavelength 330 nm, fwhm 140 nm). The spectrum of the radiation entering the cuvette was recorded using a portable UV−vis spectrometer (Ocean Optics USB4000); most of the radiation fell in the 280−400 nm window (Supporting Information, Figure S2). The reaction was monitored before and after each photolysis step with a dual-beam UV−vis spectrometer (Shimadzu UV-2450) using nanopure water in a matched cuvette as a reference. UV−vis spectra with different PA concentrations were recorded to confirm that Beer's law was obeyed (ε = 76.9 L mol^{-1} cm^{-1} at the peak of the π^* ← n transition at 280 nm; Supporting Information, Figure S3). Because the molar extinction coefficients of PA have not been published previously, we measured the average base-10 extinction coefficients and base-e cross sections of aqueous PA between 234 and 330 nm (see the Supporting Information, Figure S3 and Table S1). The quantum yield of the photolysis of PA was determined relative to that of an azoxybenzene (Fisher Scientific, 98%) actinometer.[47] In the actinometry experiment, an ethanol solution consisting of 0.2 mM azoxybenzene/6.0

mM KOH was photolyzed. The isomerization of azoxybenzene is shown in Figure S4 of the Supporting Information. The visible spectra were monitored at 458 nm, where the photoisomerization product of azoxybenzene absorbs with molar extinction coefficient ε = 7600 L mol^{-1} cm^{-1}. Details of the calibration of the spectral flux density of radiation and calculation of the quantum yield of aqueous photolysis are provided in the Supporting Information (eqs S1–S19).

B. Gas Chromatography–Chemical Ionization Mass Spectroscopy (GC–CIMS). GC–CIMS is a sensitive and highly selective technique used in this work to identify a subset of the PA photolysis products. This method cannot be applied directly to carboxylic acids such as PA because of their low volatility, so the samples were derivatized to convert the carboxyl groups into the corresponding esters prior to GC–CIMS injection. Five identical 5.00 mM PA/water solutions were prepared and photolyzed for 0, 30, 60, 90, and 120 min. The resulting solutions were derivatized by Fischer esterification to convert carboxylic acids to methyl or ethyl esters by refluxing for 1 h with methanol (Fisher Scientific, Optima, HPLC grade) or ethanol (Rossville Gold Shield), respectively, and using HCl (J. T. Baker) as a catalyst (solution pH ∼1.7). The volume of the alcohol added was roughly the same as that of the aqueous solution (few milliliters). Note that only products containing a carboxyl group are derivatized by this method; the decarboxylated products are expected to be sufficiently volatile to go through the GC column without derivatization. Cyclohexane was used to extract the ester and other nonpolar products; the volume of cyclohexane was equal to the combined volume of the H$_2$O/alcohol mixture. The cyclohexane extracts were injected into the GC–CIMS (Waters GCT-premiere, flow rate 1.5 mL/min, DB-5 30 m column, 1 μL injection amount) using the positive ion chemical ionization mass spectrometry (CIMS) mode with NH$_4^+$ as the ion reagent. The formulas corresponding to observed masses were determined by accurate mass measurements. The observed ionization mechanisms were NH$_4^+$ complexation and/or protonation. The m/z values were accurate to 30 mDa (resolving power = 7000 at m/z 200) affording determination of ion formulas. The molecular formulas of the product compounds were obtained by subtracting NH$_4^+$ or H$^+$ from the formulas of the corresponding molecular ions.

C. High-Performance Liquid Chromatography (HPLC). HPLC allows an efficient separation of the photolysis products based on their polarity. With this technique, fractions of different photolysis products of PA photolysis were isolated for further analysis. For the HPLC product separation, a 10 mM PA/H$_2$O sample was photolyzed for 60 min. Solvent A was HPLC grade water (Fisher Scientific, Omnisolv, HPLC grade) with 2% acetonitrile (EMD chemicals, HPLC grade) and 0.2% acetic acid by volume (Aldrich, 99.7%). Solvent B was acetonitrile with 0.2% acetic acid. The program was A for 5 min, linear gradient to B for 30 min, hold for 10 min, linear gradient back to A for 15 min, and hold in preparation for the next injection. The combined solvent flow rate was 1.5 mL/min. A Phenomenex Luna C18 semiprep column with a 500 μL injection loop was used for the separation. The absorption spectra of the eluent were observed in real time with a photodiode array detector (Shimadzu SPD-10Avp, 200–650 nm). A representative HPLC-PDA data run is presented in the Supporting Information, Figure S5. Fractions of different photolysis products corresponding to different retention times were collected in scintillation vials (collection time per fraction

∼20 s, of the order of the fwhm of the peaks). This procedure was repeated numerous times to collect sufficient amounts of the separated products for analysis. The collected fraction was then evaporated in a rotary evaporator at 45 °C and the residue redissolved in CD$_3$CN (Aldrich, D 99.8%, 0.03% TMS) or CDCl$_3$ (CIL, D 99.8%, 0.05% TMS) for NMR analysis (residues that were insoluble in CDCl$_3$ were dissolved in CD$_3$CN).

D. Nuclear Magnetic Resonance (NMR) Spectroscopy. The main purpose of using NMR spectroscopy in this work was to determine and/or confirm the structures of the main photolysis products. Although NMR is less sensitive than mass-spectrometry based methods, it provides important structural information that is not obtainable otherwise. A total of three different sets of NMR experiments were performed for the photolyzed products with and without separation of the products with HPLC. First, PA (Sigma-Aldrich, 98%) was dissolved in deuterium oxide to prepare four 18 mM solutions. The samples were photolyzed for 0, 15, 60, and 120 min, and their ^{1}H and ^{13}C NMR spectra were recorded using a Bruker Advance 500 MHz NMR spectrometer equipped with a highly sensitive TCI (Three Channel Inverse) cryoprobe. In the second set of experiments, CDCl$_3$ (CIL, D-content 99.8%, 0.05% TMS added) was used as the solvent to compare with aqueous photolysis, as well as to improve the signal-to-noise ratio in the NMR spectra. Four 18 mM samples were photolyzed for 0, 30, 45, and 60 min, and their ^{1}H and ^{13}C NMR spectra were recorded. Also blank experiments with photolyzed CDCl$_3$ were carried out to rule out any possible solvent photochemistry. For the third set of experiments, the photolysis products were separated using HPLC as described above and analyzed by NMR. NMR spectra of PA were also recorded in CD$_3$CN for comparison.

E. High-Performance Liquid Chromatography–Electrospray Ionization-Mass Spectrometry (HPLC–ESI-MS). The HPLC–ESI-MS instrument was used to separate and subsequently analyze the photolysis products by mass spectrometric methods. ESI-MS is a soft-ionization technique, and the low degree of fragmentation makes the spectra interpretation easier. However, ESI-MS does not provide accurate structural information; thus it was used in parallel with other analytical techniques such as NMR. An 8 mL solution of 10 mM PA/H$_2$O (Fisher Scientific, Omnisolv, HPLC grade) was photolyzed for 60 min and concentrated by evaporation from 8 to 4 mL. The sample was injected into an HPLC–ESI-MS instrument (Waters LCT Classic, LC is an Agilent 1100 and the autosampler is a Gilson 231XL) and both positive (+) and negative (−) ion mode mass spectra were recorded using a 25 cm × 2 mm Luna C18(2), 3 μm particles, column. The injection amount was 10 μL and the flow rate was 0.2 mL/min. A mass range of 100–1000 was covered with both modes. The solvents (A, B) were the same as described in the HPLC-PDA section, and the gradient program used was A for 1 min, linear gradient to B for 50 min, hold for 7 min, linear gradient back to A for 3 min, and hold in preparation for the next injection. The similarity in the solvents, gradient programs, and column stationary phases made it straightforward to cross-correlate peaks in the HPLC-PDA and HPLC–ESI-MS chromatograms. The observed ionization mechanisms were Na$^+$ addition and/or protonation in the (+) mode and deprotonation in the (−) mode. Chromatograms of PA and the HPLC-separated main photolysis product (PA isomer) were also recorded for comparison.

F. Gas-Phase Photolysis. We attempted to study gas-phase photolysis of PA but its relatively low volatility resulted in poor signal-to-noise in the measurements. Therefore, PA methyl ester (hereafter abbreviated as PAMe) was investigated instead of PA in our experiments. The substitution of the carboxyl group by its ester assumes that the carboxyl group is not the main participant in the photolysis mechanism. PAMe was prepared by esterification of PA with methanol, as described above. The cyclohexane extract was evaporated, resulting in a clear liquid containing PAMe and some residual PA. The gas-phase photolysis setup (Figure S6 in the Supporting Information) consisted of a 230 L Teflon FEP bag with several feed-through inlets. Ten microliters of PAMe/cyclohexane solution was injected into a separate 9 L Teflon bag and evaporated into the main bag with 8−10 SLM flow of dry air (this was done to avoid issues with introducing the liquid ester into the photolysis bag). The concentration of the ester was monitored in real time with a proton-transfer-reaction time-of-flight mass spectrometer (PTR-ToF-MS, Ionicon Analytik). After the ester concentration had stabilized, the content of the bag was photolyzed for 4 h using a bank of 10 Philips UV−B lamps (TL 40W/12 RS). The emission spectrum of the lamps is shown in the Supporting Information, Figure S7. The quantum yield of the PA methyl ester photolysis was determined by using acetone actinometry (eqs S20−S23 in the Supporting Information). Acetone cross sections were used in lieu of the gas-phase PAMe cross section in the quantum yield calculations (because the latter are not known). Gas-phase acetone absorption cross sections and photolysis quantum yields required for the calculation were taken from the 2011 version of the NASA JPL evaluation of "Chemical Kinetics and Photochemical Data for Use in Atmospheric Studies".[48]

III. COMPUTATIONAL METHODS

Semiempirical on-the-fly calculations simulating PA photolysis in the gas phase and in small water clusters were performed to gain additional insights into the mechanism. The aqueous solution was modeled by using complexes of PA with one or five water molecules. Solvation by five water molecules is admittedly not a realistic model of an aqueous environment (more than 500 water molecules would be required for the completion of several solvation shells). However, it should be adequate for qualitatively testing the effect of solvent molecules on photochemistry. Indeed, past studies demonstrated that already one water molecule can have a large effect on the photolysis dynamics.[49−58] It would certainly be of great interest to model the hydrated PA system by a larger cluster, but this is currently not computationally feasible. A comparison of the results of calculations for PA hydrated with zero, one and five molecules should provide a trend for the effect of the solvent, a strategy that proved to be useful in previous studies.

In these simulations, classical trajectories are computed to describe the reaction process in time. The reliability of the potential surface used is of critical importance. On the basis of our experience with related processes, a semiempirical Orthogonalization-corrected Method 2 (OM2)[59] was used. The efficiency of the method made possible the calculation of a substantial set of trajectories (100) sufficient to have good statistics for different reaction channels. For the hydrated systems, calculations were done for the PA methyl ester (PAMe) instead of PA. This substitution prevents the carboxyl group of PA from drawing water molecules away from the carbonyl group on the opposite end of the molecule, where

photochemistry is initiated. As the main focus of this work is on the carbonyl-driven photochemistry of PA, the interactions of the water molecules with the carboxyl group are of lesser interest. The carboxyl group is sufficiently isolated, and the PA→PAMe substitution should not have a strong effect on the photodissociation dynamics.

The structure of bare PA and the structure of PAMe with one or five water molecules were optimized in the singlet ground state with the second-order Møller−Plesset perturbation theory (MP2) using the cc-pVDZ basis set.[60] The resolution-of-identity (RI) approximation[61] for the evaluation of the electron-repulsion integrals implemented in Turbomole[62] was utilized, and the excitation energies were calculated using the algebraic diagrammatic construction method 2 (ADC(2)).[63] The PA and PAMe/water systems cannot be treated by high-level ab initio methodology in a dynamical approach due to their large size. On the other hand, classical force fields that are commonly used for simulating the dynamics of larger systems up to the size of protein molecules are unable to treat electronic excitations and bond breaking and formation. Therefore, a semiempirical potential energy surface was chosen to treat the photodissociation dynamics. The potential energy surface calculations were performed using semiempirical OM2 and OM2/MRCI (multireference configuration interaction) methods.[64] This method was chosen on the basis of its success with treating photodissociation of similar systems in the past.[51,65,66] Most important in this reaction's context is the success of the method in describing Norrish-I and Norrish-II reactions in pentanal, processes relevant also here.[66] In the OM2 method, proper orthogonality of the orbitals has been introduced, which leads to a better description of energy barriers between different conformers. A related semiempirical method Parameterized Model number 3 (PM3),[67−70] has been previously used for the dynamics calculations for atmospherically relevant systems.[71,72] Most of the semiempirical methods were constructed for the use of static and dynamical ground-state calculations and therefore lack the ability to sufficiently treat excited states. OM2 is advantageous when compared to PM3 and other semiempirical methods because the excited states can be treated by an equivalent excited-state method OM2/MRCI. With the OM2/MRCI method, multireference systems can be treated by using several configurations for a particular state. Excitations from these configurations are additionally computed. Those configuration-state functions, each with its proper weight, constitute the overall wave function of the system. In the OM2/MRCI calculations employed here, three reference configurations were used (closed shell and single and double HOMO−LUMO excitations). The active space was chosen to include the highest five occupied orbitals and the lowest five unoccupied orbitals for PA and hydrated PAMe. The active space for all these systems was chosen on the basis of comparison to the orbital excitations in the ADC(2) calculations.[63]

Simulation of photoinduced processes in PA and hydrated PAMe (one or five water molecules added) were carried out via excited-state dynamics calculations utilizing the semiempirical Modified Neglect of Diatomic Overlap (MNDO) program.[73,74] The simulation consisted of three steps: (1) ground-state dynamics to sample the initial configurations; (2) vertical transition to the first excited singlet-state S_1 and intersystem crossing (ISC) from S_1 to the lowest triplet-state T_1; (3) dynamics on T_1. A schematic diagram of the simulation approach is presented in Figure 1 of ref 66, which focused on

the dynamics of pentanal photolysis. In contrast to the pentanal study, the excited-state dynamics on the singlet-state surface was omitted in the PA and PAMe case. The S_1 to T_1 gap was directly computed on structures obtained by the ground-state dynamics (step 1). The omission of S_1 from the dynamics is certainly an approximation as some carbonyls are known to be photolyzed in the singlet excited states.[75] Our recent theoretical study of pentanal by similar methods has explored the potential importance of dissociation in the S_1 state.[66] A test simulation of 17 ps was carried out on the excited S_1 state of pentanal and no reactions occurred in this time. In addition, a large ensemble of trajectories for a shorter time scale was tested with the same conclusion. Because of the fact that the photodissociation dynamics were faster in the T_1 state, we do not expect a significant error from excluding S_1 from the photodissociation dynamics calculations for PA and PAMe.

The sampling for the initial condition was determined by running a trajectory on the ground electronic state for 10 ps at 300 K using the velocity–Verlet algorithm with a 0.1 fs time step and utilizing the OM2 potential. For PAMe with one or five water molecules, the temperature was set to 200 K to prevent evaporation of water molecules.

The significance of triplet electronic states in the photolysis of carbonyls is well established.[75] It was assumed that PA or PAMe would go through ISC from the S_1 to the T_1 state before undergoing any photochemical changes. A number of theoretical approaches have been developed to describe the ISC process,[76−80] with Tully's nonadiabatic surface-hopping dynamics[81] applied in most of these approaches. The singlet-to-triplet gap energies along the ground-state trajectory were evaluated by calculating the singlet and triplet energies on 1000 structures. However, the ISC process is generally slow (time scale ~10^{-8} s) and a dynamical approach utilizing on-the-fly electronic structure calculations would be computationally too expensive. Because the main goal of the work was not to study the ISC event, but rather to concentrate on the photochemistry, a more simplified approach was chosen. It was assumed that ISC (eventually) takes place at the geometries where the singlet-to-triplet energy gap is the smallest. The energy gap range was 0.51−0.56 and 0.37−0.89 eV for PA and for hydrated PAMe, respectively. These geometries were then used as the starting point for the triplet-state dynamics. A similar approach was previously used in dynamics starting from a conical intersection or top of a reaction barrier.[82,83]

A total of 100 geometries with the smallest singlet-to-triplet gaps were chosen as initial conditions for the dynamics on the T_1 state. Experience with simulations for pentanal indicates that such a number of trajectories is essential for describing the different reaction channels involved. Thermal equilibrium was assumed to be reached immediately after the ISC event, because vibrational relaxation is generally faster. On the basis of this assumption, Monte Carlo sampling of kinetic energy, which can be converted to an equivalent temperature of 300 K, was used to create the initial velocity of the atoms. The adiabatic dynamics were run for 100 ps and one trajectory was run from every starting geometry. For PAMe, the dynamics were also tested at 200 K. The cleavage distance for the C−C_α bond breaking was assumed to be 2.5 Å. At this distance, the chemical interaction between the fragments is negligible.

IV. RESULTS AND DISCUSSION

A. Mechanism of Photolysis. Figure 1 shows the GC−CIMS total-ion-current chromatograms of the PA aqueous
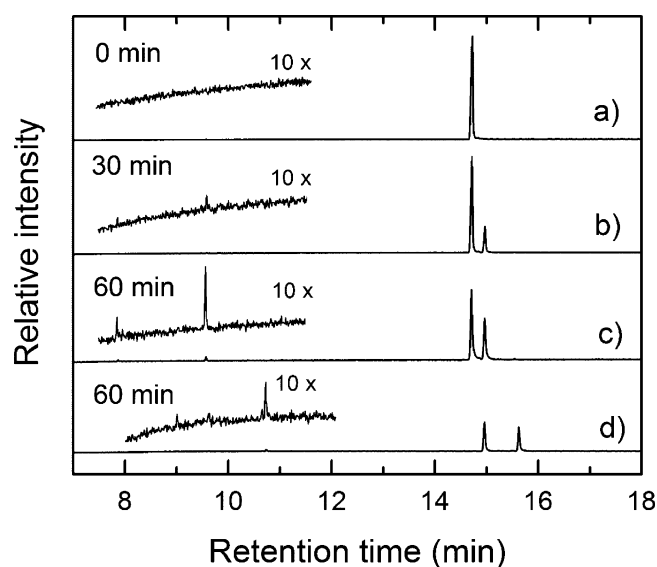
Figure 1. GC−CIMS total-ion-current chromatograms: (a)−(c) PA after 0, 30, and 60 min aqueous photolysis followed by esterification of the photolysis products with methanol; (d) PA after 60 min aqueous photolysis followed by esterification of the photolysis products with ethanol. The insets show magnified portions of the chromatogram relative to the same x-axis.

photolysis products after 0, 30, and 60 min irradiation and esterification with methanol in panels a−c, respectively. A chromatogram taken after 60 min irradiation and esterification with ethanol is presented in panel d. The observed formulas are listed in Table 1. Before photolysis, only the PAMe peak is visible at 14.7 min retention time detected as $C_{11}H_{18}O_3-NH_4^+$ and as $C_{11}H_{18}O_3-H^+$ (the chemical formula of PA is $C_{10}H_{16}O_3$, but esterification of PA with methanol converts it into $C_{11}H_{18}O_3$). After 30 min of irradiation, one major product peak is visible around 15.0 min retention time, corresponding
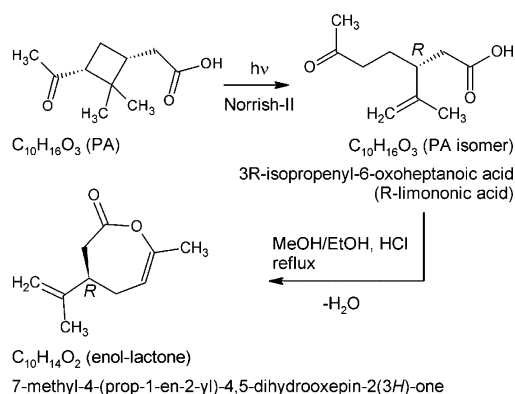
Table 1. Molecular Formulas and Nominal Masses of Observed Products of the Aqueous Photolysis of PA[a]

molecular formula (nominal mass, Da)	detection method	mechanism
$C_6H_{10}O_2$ (114)	GC−CIMS, HPLC−ESI-MS	ring opening
$C_8H_{14}O_2$ (142)	GC−CIMS, HPLC−ESI-MS	Norrish-I
$C_8H_{12}O_3$ (156)	HPLC−ESI-MS	Norrish-I, Norrish-II
$C_9H_{16}O_2$ (156)	HPLC−ESI-MS	Norrish-I
$C_8H_{12}O_4$ (172)	HPLC−ESI-MS	Norrish-I
$C_8H_{14}O_4$ (174)	HPLC−ESI-MS	Norrish-I
$C_{10}H_{16}O_3$ (184)	GC−CIMS, HPLC−ESI-MS	Norrish-II, major product
(200)	HPLC−ESI-MS	unknown
(206)	HPLC−ESI-MS	unknown
(224)	HPLC−ESI-MS	unknown
(226)	HPLC−ESI-MS	unknown

[a]The formulas of the impurities seen in Figure 2a in the initial solution are not included in the list. For consistency, the formulas from the GC−CIMS measurements correspond to the photolysis products before esterification with methanol or ethanol. The mechanism column indicates whether the product is formed by the Norrish type I (Scheme 3), Norrish type II (Scheme 2), or direct ring-opening (Scheme 2) pathway. The major detected product is $C_{10}H_{16}O_3$, a Norrish type II isomer of PA shown in Schemes 1 and 2.

to a chemical formula of $C_{10}H_{14}O_2$, detected as $C_{10}H_{14}O_2-$ $NH_4^+/C_{10}H_{14}O_2-H^+$. In the case of esterification with ethanol, the PA ethyl ester peak elutes at 16.0 min, but the major product peak at 15.0 min remains at the same position, suggesting a product that is not dependent on the alcohol during the esterification. We propose that the major photolysis pathway of PA leads to its structural isomer, 3-isopropenyl-6-oxoheptanoic acid (CAS Registry No. 4436-82-2), also known as limononic acid, formed by the Norrish type II splitting that opens the cyclobutane ring of PA (Scheme 1). Strictly speaking,

Scheme 1. Major Observed Photolysis Pathway for PA, Resulting in a Norrish Type II Isomerization into 3-Isopropenyl-6-oxoheptanoic Acid (Referred to as Limononic Acid or PA Isomer in the Text)[a]


$C_{10}H_{16}O_3$ (PA)

$C_{10}H_{16}O_3$ (PA isomer)
3R-isopropenyl-6-oxoheptanoic acid
(R-limononic acid)

MeOH/EtOH, HCl
reflux
$-H_2O$

$C_{10}H_{14}O_2$ (enol-lactone)
7-methyl-4-(prop-1-en-2-yl)-4,5-dihydrooxepin-2(3H)-one

[a]The intramolecular esterification of the enol form of the PA isomer produces the enol−lactone detected by the GC−CIMS method (Figure 1). The methods used in this paper are not sensitive to the stereochemistry of the products; expected enantiomers are shown for reference.

on the basis of the mechanism, we expect the *R*-stereoisomer of limononic acid, indexed under a separate CAS Registry No. 174746-84-0 but the methods used in this paper cannot distinguish stereoisomers. A single dominant product of PA photolysis is in agreement with the HPLC−PDA, HPLC−ESI-MS, NMR, and UV−vis results, as we will discuss below. The existence of this photolysis channel is also supported by the calculations. The $C_{10}H_{14}O_2$ molecule observed in the GC−CIMS experiments must be produced via intramolecular esterification of the PA isomer under the acidic refluxing conditions. The resulting cyclic enol−lactone shown in Scheme 1 can be formed from the isomer but apparently not from PA itself due to the more rigid structure of the latter.

In addition to the major product, minor products are also observed in GC−CIMS measurements. After 60 and 90 min, two small additional peaks elute at 8 and 10 min retention times, detected as $C_9H_{16}O_2-NH_4^+/C_9H_{16}O_2-H^+$ and $C_7H_{12}O_2-NH_4^+/C_7H_{12}O_2-H^+$. Both of these peaks shift by ~1 min when ethanol is used instead of methanol in the esterification step. Therefore, we assume that the peaks are esters of carboxylic acids corresponding to nonesterified formulas $C_8H_{14}O_2$ and $C_6H_{10}O_2$, respectively. These species are also observed in the HPLC−ESI-MS experiments described below. After 2 h of photolysis, two smaller additional peaks appeared in the chromatogram, corresponding to $C_{10}H_{14}O_2$, detected as $C_{10}H_{14}O_2-NH_4^+/C_{10}H_{14}O_2-H^+$. This is coincident with the PA isomer formula, and these species likely correspond to two less abundant isomers of PA (as will be discussed below, Norrish type II splitting of PA can go by three different routes with the one shown in Scheme 1 being most favorable in the steric sense).

Sample HPLC−ESI-MS data are presented in Figure 2, and observed formulas are listed in Table 1, along with the species
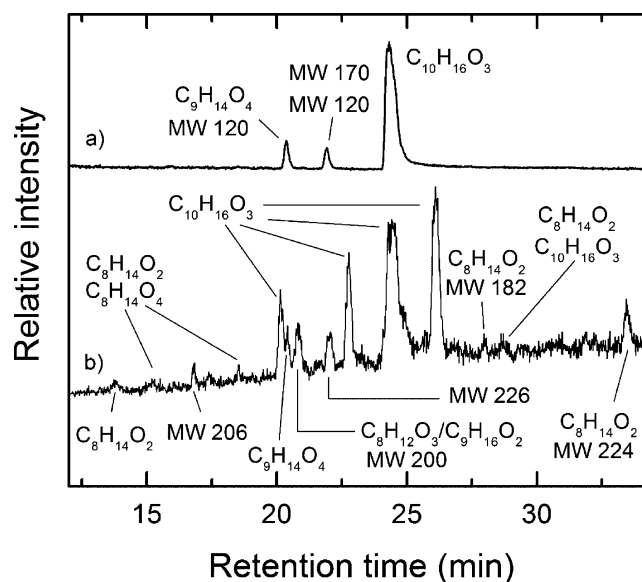

Figure 2. HPLC−ESI-MS (−) ion mode total-ion-current chromatograms: (a) PA solution before photolysis; (b) PA solution after 30 min photolysis. Chromatographic peaks are labeled by the molecular formula(s) and/or nominal mass(es) of the neutral compounds corresponding to the major observed ions.

detected by GC−CIMS. The (−) ion mode resulted in more easily interpretable peaks because of the ease of deprotonation of carboxylic acids. Assignment of the (+) ion mode data was complicated by dimer formation and interference from solvent peaks, and it is not discussed in this work. Figure 2a suggests that the initial PA solution contained impurities resulting in peaks corresponding to $C_9H_{14}O_3$ (170), and $C_9H_{14}O_4$ (186). $C_9H_{14}O_4$ is likely pinic acid, which has high ionization efficiency in the (−) mode spectra, and even small amounts of impurity may result in observable peaks. Because pinic acid does not contain carbonyl groups, we do not expect it to directly participate in photolysis.

The products growing upon photolysis in the ESI-MS (−) data (Table 1) can be interpreted with the help of mechanisms suggested for photolysis of similar systems such as cyclobutyl methyl ketone, aliphatic ketones, etc.[10,38−43,84] The well-known carbonyl splittings via Norrish type I and Norrish type II reactions explain most of the products that were observed.[85] Norrish type I splitting of carbonyls is the major path for small (C1−C5) carbonyls, and Norrish type II splitting dominates in larger carbonyls with available hydrogen atoms in the *γ*-position relative to the carbonyl group. The suggested reaction mechanisms for the aqueous photolysis of PA are presented in Schemes 2 and 3.

The Norrish type II reaction starts with the 1,5-shift of a hydrogen atom to the excited carbonyl group. Scheme 2 shows that this shift can go via two pathways, with pathway a being less sterically hindered than pathway b. The biradical formed after the 1,5-shift further isomerizes by the cyclobutane ring-opening, producing three possible PA isomers. We suggest that the isomer formed by pathway a, i.e., limononic acid, is the

Scheme 2. Photolysis Products Expected from the Norrish Type II Splitting (Pathways a and b) and Direct Ring Opening (Pathway c) of PA in an Aerated Solution[a]
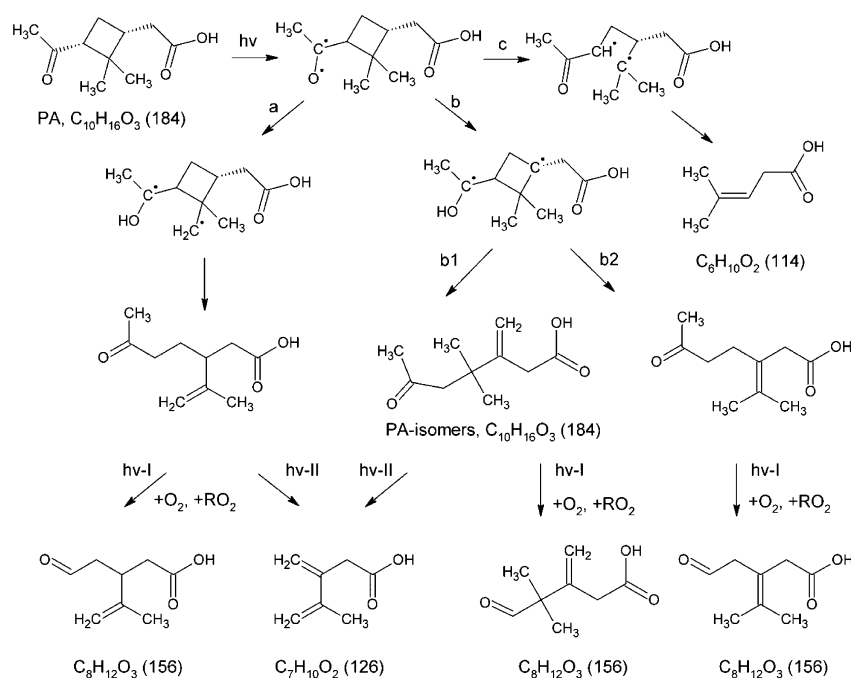
[a]Possible secondary photolysis pathways for the PA isomers are also shown (hv-I and hv-II stand for Norrish type I and type II mechanisms, respectively).

Scheme 3. Products Expected from the Norrish Type I Splitting of PA and Secondary Chemistry of the Resulting Free Radicals in an Aerated Solution

12936

dx.doi.org/10.1021/jp4093018 | J. Phys. Chem. A 2013, 117, 12930–12945
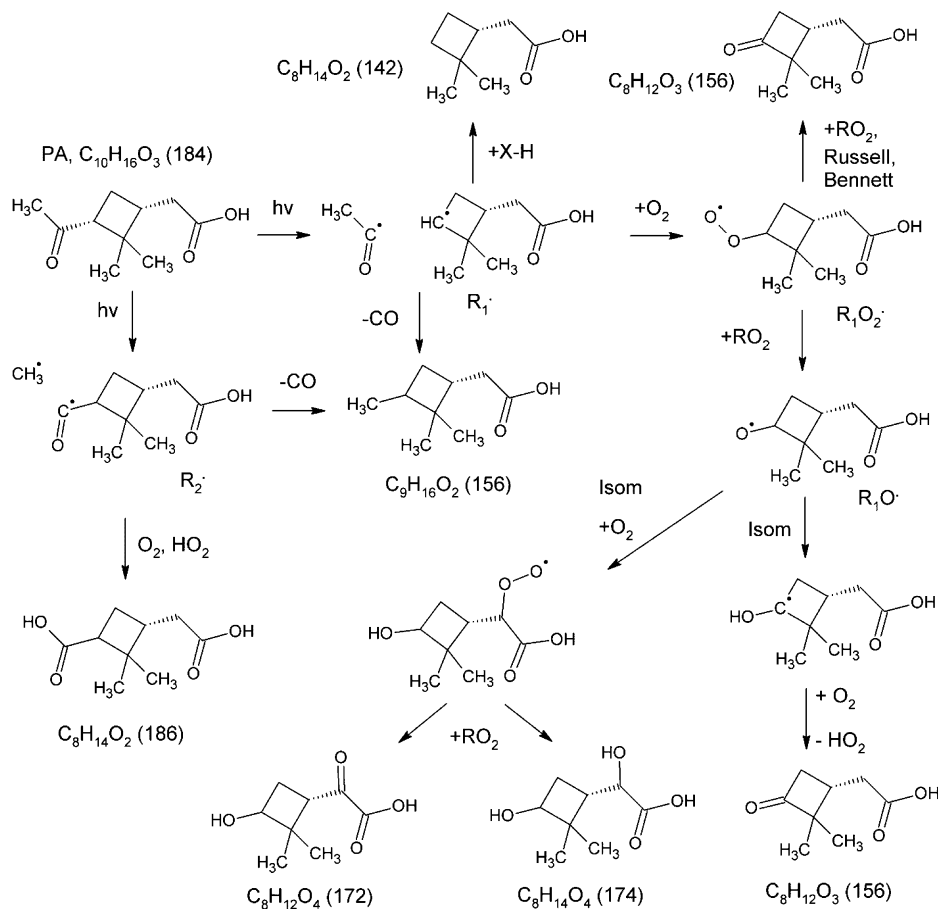
major photolysis product because the methyl group supplying the hydrogen atom is ideally positioned with respect to the carbonyl group for the efficient 1,5-shift (this assumption is supported by the calculations described below). Two more isomers are formed via pathways b1 and b2 through less probable 1,5-shifts due to steric constraints. HPLC−ESI-MS data provides evidence that all three isomers are formed in photolysis (Figure 2), but the GC−CIMS data clearly show that only one of them dominates. All three PA isomers possess a carbonyl group and can be further photolyzed via secondary Norrish type I and Norrish type II reactions, as shown in Scheme 2. One of the predicted secondary photolysis products is detected in the HPLC−ESI-MS experiments as $C_8H_{12}O_3$ (156, the numbers in parentheses refer to the nominal molecular weight of the compound). A non-Norrish radical rearrangement pathway c that leads to a direct cyclobutane ring-opening and further splitting of the molecule was previously observed by Baldwin et al. for cyclobutyl methyl ketone,[38] and it can lead to a product formation with the formula $C_6H_{10}O_2$ (114), which is also observed in our experiments as a minor product.

The HPLC−ESI-MS offers evidence that Norrish type I reactions also occur in solution but to a lesser extent than Norrish type II reactions. The Norrish type I splitting can proceed via two different channels via formation of $CH_3\overset{\bullet}{C}(O)$ or $CH_3^\bullet$ and the corresponding residual radicals $R_1^\bullet$ and $R_2^\bullet$ (Scheme 3). In either case, the geminate pair of radicals can disproportionate in the solvent cage with a loss of CO and formation of a stable product $C_9H_{16}O_2$ (156). If radical $R_1^\bullet$ encounters a suitable hydrogen atom donor, a product with formula $C_8H_{14}O_2$ (142) may result. In an aerated solution, the initially produced free radicals $R_1^\bullet$ and $R_2^\bullet$ quickly recombine with O_2, leading to long-lived peroxyl radicals $RO_2^\bullet$. The equilibrium concentration of dissolved oxygen in water is ~0.2 mM, i.e., smaller than that of PA (18 mM in most experiments), but the diffusion-limited rate constant for the $R^\bullet$ and O_2 recombination is larger than the expected rate constant for abstraction of a hydrogen atom from PA by $R^\bullet$. The peroxyl radical $R_2O_2^\bullet$ eventually forms pinic acid $C_9H_{14}O_4$ (186) along with other products. The peroxyl radical $R_1O_2^\bullet$ can be removed through self-reactions (Bennet, Russell),[84] forming a cyclobutanone derivative with formula $C_8H_{12}O_3$ (156). Alternatively, $R_1O_2^\bullet$ can be converted to alkoxy radical $R_1O^\bullet$, which upon further isomerizations and reactions produces products with formulas $C_8H_{12}O_4$ (172), $C_8H_{14}O_4$ (174), and $C_8H_{12}O_3$ (156). Though the products with formula $C_8H_{12}O_3$ (156) can also be formed via the Norrish type II pathways (Scheme 2), the products $C_8H_{14}O_2$ (142), $C_9H_{16}O_2$ (156), $C_8H_{12}O_4$ (172), and $C_8H_{14}O_4$ (174) are unique to Norrish type I splitting, and their observation in the HPLC−ESI-MS data confirms that both type I and II reactions occur in parallel. The resolving power of the ESI-MS instrument was not high enough to unambiguously distinguish between $C_8H_{12}O_3$ (156) and $C_9H_{16}O_2$ (156), but the peak positions were more consistent with the latter formula. Measurements of the gas-phase photolysis products of PAMe with a PTR-ToF-MS indicate the presence of both of the analogous methyl-esterified isomers: $C_9H_{14}O_3$ (171) and $C_{10}H_{18}O_2$ (171).

NMR spectra were recorded to confirm the structures of the products. The NMR data are summarized in Table S3 of the Supporting Information. The ^1H and ^{13}C NMR spectra of PA were in good agreement with the literature.[86] The HPLC-separated fraction corresponding to the major photolysis

product was identified as 3-isopropenyl-6-oxoheptanoic acid (limononic acid), as shown in Scheme 1. The literature NMR spectrum of limononic acid has not been previously reported, so we compared it with its predicted ^1H and ^{13}C spectra from ref 87. To validate the accuracy of such predictions, we did the same calculations for the PA itself. The predicted NMR results for PA were in relatively good agreement with our previously reported experimental results, and the small discrepancies seen in the PA comparison were comparable to what we see in the experimental vs calculated PA isomer results. The other HPLC-separated fractions produced lower-quality NMR spectra due to low concentration and interference from PA and/or the isomer, and the structures were not reliably identifiable. The 60 min photolysis experiment carried out in chloroform (instead of water) produced an especially clear ^{13}C spectrum with good S/N, from which it was possible to distinguish both PA and its isomer peaks (Figure S8 in the Supporting Information). The NMR results support the assumption that limononic acid is the dominant photolysis product, both in water and in chloroform.

B. Absorption Cross Sections and the Photolysis Quantum Yield of PA. No absorption cross section data have been previously published for PA in any solvent. We measured the aqueous PA molar extinction coefficients and converted them into absorption cross sections (Table S1 in the Supporting Information). The cross sections of gas-phase acetone,[48] cyclobutyl methyl ketone in isooctane,[38] aqueous acetone,[88] and aqueous PA are compared in Figure 3. The PA
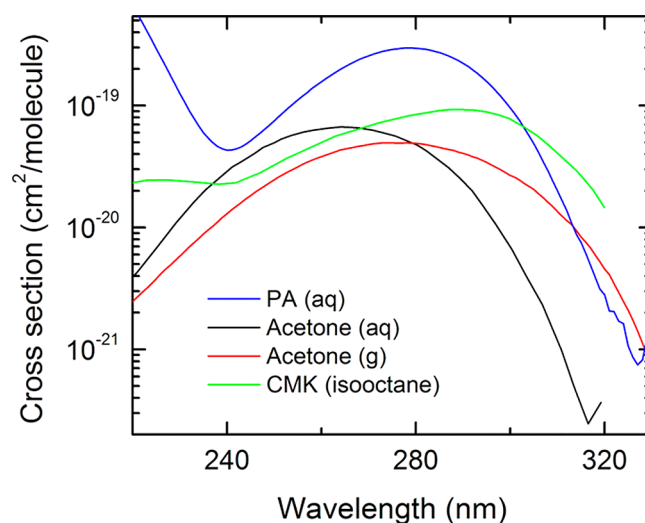

Figure 3. Absorption cross sections of aqueous PA (this work, used for calculating the quantum yield of photolysis in aqueous experiments), aqueous acetone,[88] gas-phase acetone (used for calculating the quantum yield of photolysis in gas-phase experiments),[48] and cyclobutyl methyl ketone in isooctane.[38]

cross sections have the largest value in the middle of the $\pi^* \leftarrow n$ band, which is a result of two effects. First, a cyclobutyl ring adjacent to a carbonyl group increases the absorption coefficient, a consequence of hyperconjugation.[89] This effect accounts for the increase between the cross sections of aqueous acetone and aqueous PA. Second, there is a blue shift and an increase in the cross sections upon solvation in polar solvents compared to nonpolar solvents.[90] This effect is clearly observed from comparison of absorption spectra of PA in water and cyclobutyl methyl ketone in isooctane. Ideally, Figure 3 should have included absorption cross sections of gas-phase PA or

PAMe but we could not perform these measurements quantitatively. In the following discussion, we will use the measured absorption cross sections of aqueous PA for all aqueous photolysis calculations, and approximate the absorption cross sections of gas-phase PA and PAMe with those of gas-phase acetone.

The absorption spectra of the 0.2 mM azoxybenzene actinometer and 18 mM PA at different photolysis times are shown in Figures 4 and 5, respectively. The PA's 280 nm $\pi^* \leftarrow$
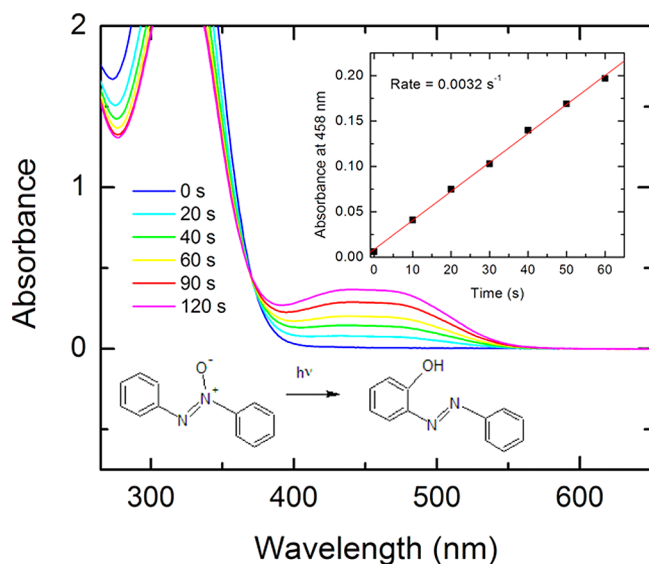
Figure 4. UV−vis spectra of the azoxybenzene actinometer taken after different photolysis times under the same conditions as the photolysis of PA. The measured photoisomerization rate of the actinometer and its known quantum yield are used to obtain the quantum yield of photolysis of PA.
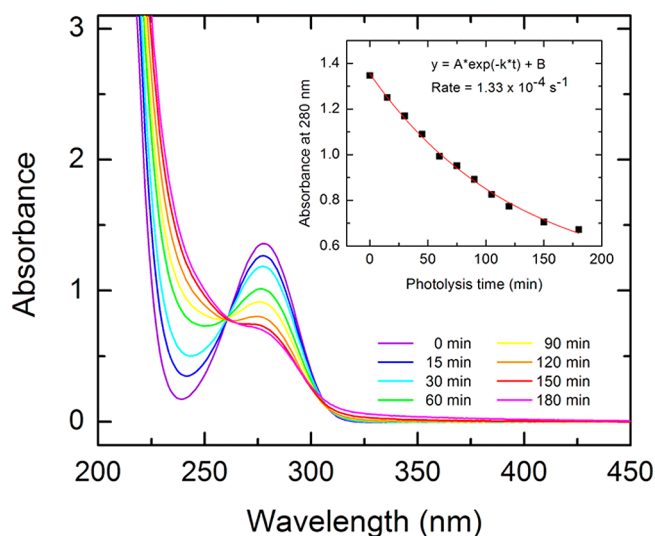
Figure 5. UV−vis spectra taken during aqueous photolysis of an 18 mM PA solution. The inset shows an exponential fit to the absorbance at 280 nm as a function of time using Model 1.

n carbonyl peak decreases as a function of photolysis time, and the presence of a clearly defined isosbestic point at 260 nm suggests that only one photolysis product has significant absorbance in this spectral window. After 2.5 h of photolysis, most of the initial PA absorbance has disappeared, and further

photolysis does not change the absorption spectrum of the mixture significantly, suggesting that the terminal product(s) are stable with respect to photolysis. The carboxyl functional group of PA is isolated from the carbonyl group by a chain of sp^3 carbon atoms. Isolated carboxyl groups do not absorb enough radiation at relevant experimental and atmospheric wavelengths to induce photochemistry. However, as we will see below, the carboxyl group can "steal" some of the excitation energy from the carbonyl group leading to decarboxylation. This highlights the importance of studying photochemistry of multifunctional molecules with a relevant distribution of functional groups.

The inset in Figure 5 shows the base-10 absorbance of the solution at the peak of the $\pi^* \leftarrow$ n band at 280 nm as a function of photolysis time. Three distinct kinetics models were used to describe the observed time dependence. The photolysis rate fits are limited to early times to suppress the effect of secondary photolysis. Model 1 assumes an idealized case of a single nonphotolyzable product (P) of photolysis of PA. In Model 1, the time dependence of the absorbance should be described by the following equation,

$$A_{10}(t) = A_0[\beta + (1 - \beta) \cdot e^{-k_{PA} \cdot t}] \tag{1}$$

where A_0, β, and k_{PA} are fitting parameters (Supporting Information eqs S24−S28). The physical meaning of parameter β is the ratio of the 280 nm molar extinction coefficient of the photolysis product P to that of PA, $\beta = \varepsilon_P/\varepsilon_{PA}$, and parameter A_0 is the initial absorbance of the solution. The fit to eq 1 results in the photolysis rate constant of $k_{PA} = 1.33 \times 10^{-4}$ s^{-1} (in the example shown in Figure 5). A comparison with the rate of photolysis of the actinometer makes it possible to calculate the photolysis quantum yield for the loss of PA, as described in detail in the Supporting Information. Table 2 summarizes the results of independent measurements of the photolysis quantum yields based on Model 1, with the average result equal to 0.43 ± 0.09(1σ).

Table 2. Measured Photolysis Quantum Yields of Aqueous PA (a) and Gas-Phase PAMe (b)[a]

(a) Aqueous PA		
concentration (mM)	quantum yield (Model 1)	quantum yield (Model 3)
18	0.32 ± 0.03	0.39 ± 0.08
10	0.49 ± 0.03	0.93 ± 0.19
2.0	0.47 ± 0.06	0.64 ± 0.24
average	0.43 ± 0.09	0.65 ± 0.27
(b) Gas-Phase PAMe		
measurement		quantum yield
gas-phase 1		0.51 ± 0.06
gas-phase 2		0.55 ± 0.06

[a]The stated uncertainties of the aqueous photolysis values are propagated from the uncertainties of the fitted parameters k_{PA} in Models 1 and 3. The uncertainties in the gas-phase values are similarly propagated from the fitted first-order loss rate constants.

The primary photolysis pathway for PA is Norrish type II isomerization, with the limononic acid product still retaining the $-C(O)CH_3$ group. Furthermore, the HPLC and GC measurements suggest that a number of minor products of photolysis are also produced, some of which are photolyzable as well. Therefore, Model 1, which assumes a single nonphotolyzable product may not be appropriate in this case.

Model 2 assumes a two-step process, PA → IS → P, wherein IS stands for the PA isomer (limononic acid) and P designates terminal product(s). Model 2 further assumes that the photolysis rate constants for the PA → IS and for IS → P steps are roughly the same ($k_{PA} \approx k_{IS}$), and that the 280 nm molar extinction coefficients of PA and IS are similar in magnitude ($\varepsilon_{PA} \approx \varepsilon_{IS}$). These assumptions are inspired by the similarity in the shapes of the absorption spectra of PA (Figure 5) and its isomer (Figure S5 in the Supporting Information). With these approximations, the solution for the 280 nm absorbance of the solution becomes (see Supporting Information eqs S29−S36 for the derivation):

$$A_{10}(t) \approx A_0[\beta + (1 - \beta)(1 + kt) \times e^{-k \cdot t}] \quad (2)$$

where A_0, β, and k_{PA} are fitting constants and β has the same physical meaning as in Model 1. An isosbestic point is still predicted to occur in this kinetics model. We find that Model 2, despite its more realistic assumptions, does not fit the data as well as Model 1 does. The effect of the linear term in the pre-exponential factor is to make the time dependence sigmoidal (because at early times PA is simply replaced by its equally absorbing isomer), and this is not borne out by the observations.

Model 3 takes into account the fact that the cyclobutyl ring is known to significantly increase the excitation coefficient of an adjacent carbonyl group.[89] This model also assumes a two-step process, PA → IS → P, but both the 280 nm molar extinction coefficient and the photolysis rate of IS are reduced by a certain constant factor ($f = 0.16$) relative to that of PA: $k_{IS} = f \times k_{PA}$ and $\varepsilon_{IS} = f \times \varepsilon_{PA}$. The value of f was estimated from comparison of the peak $\pi^* \leftarrow n$ cross sections of aqueous PA (which has an absorbance-enhancing cyclobutyl ring) and aqueous acetone (which does not) shown in Figure 3. These assumptions lead to the following equation (Supporting Information eqs S37−S41):

$$A_{10}(t) = A_0\left[\beta + \frac{(1 - 2f) + f\beta}{1 - f}e^{-k_{PA} \cdot t} + \frac{f - \beta}{1 - f}e^{-f \cdot k_{PA} \cdot t}\right] \quad (3)$$

No isosbestic point is expected in Model 3; however, certain combinations of f and β can result in a situation resembling the isosbestic behavior observed in our experiments. Fitting the observations to eq 3 with parameter f fixed at 0.16 resulted in the quantum yields for PA photolysis listed in the last column of Table 2. The average quantum yields obtained from Models 1 and 3 are 0.43 ± 0.09 and 0.65 ± 0.27, respectively. The experiments were performed using three different concentrations, and no qualitative differences between the resulting values of the quantum yields were observed. The spread in the results of the two models reflects the inherent uncertainty of the experimental method, which relies on the UV−vis measurements of the total absorbance of the solution containing both the PA and its photolysis products. Despite these uncertainties, we can confidently state that roughly half of the photons absorbed by aqueous PA lead to its isomerization or decomposition. We recommend a value of 0.5 ± 0.3 for the quantum yield of aqueous PA photolysis, with the large errors conservatively chosen to account for the uncertainties in the data fitting models.

Gas-phase photolysis of PAMe was investigated for comparison with the aqueous PA. Acetone was used as an actinometer, and the wavelength dependence of its photolysis quantum yield and absorption cross sections was explicitly

taken into account in the calculations.[48] The removal of PAMe and acetone during gas-phase photolysis observed with the PTR-ToF-MS instrument are shown in Figure S9 of the Supporting Information. The decays are well described by single exponential loss, and direct comparison of the first-order decay rates produces a quantum yield of 0.53 ± 0.06 for the photolytic removal of gas-phase PAMe. However, the quantum yields for the aqueous and gas-phase photolysis should be compared with caution. The gas-phase quantum yield does not account for the Norrish type II isomerization, and therefore its value represents the lower limit for the total quantum yield of PAMe photolysis. An isomerization of gas-phase PAMe, analogous to the isomerization observed for aqueous PA (Scheme 1) leading to the methyl ester of limononic acid would not be detectable by PTR-ToF-MS, because the reactant and product molecules are isobaric.

The PTR-ToF-MS mass spectra also provided information about possible products of photolysis, although the interpretation was complicated by the fragmentation of the protonated ions in the PTR source. A comparison of the observed mass spectra obtained before and after photolysis is shown in Figure S10 of the Supporting Information. Figure S11 shows the difference mass spectrum to highlight the masses that appear and disappear during photolysis. The time-series plot showing the disappearance of PAMe and the formation of select products as a function of photolysis time is presented in Figure S12 (Supporting Information). It was observed that the Norrish type I products of PAMe photolysis, $C_9H_{14}O_3$ (170.084) and $C_{10}H_{18}O_2$ (170.131), analogues of the two MW = 156 products observed in the photolysis of aqueous PA (Scheme 2 and 3), each increased upon photolysis. Increases in $C_8H_{12}O_2$ (140.084) and $C_9H_{16}O_4$ (188.105) also occurred during gas-phase photolysis of PAMe. The aqueous PA photolysis analogue of the former product would be $C_7H_{10}O_2$ (126). This species was not observed in the LC−ESI-MS experiments with photolyzed aqueous PA but was expected on the basis of the suggested mechanism (Scheme 2). The aqueous PA photolysis of the $C_9H_{16}O_4$ (188.105) product would be $C_8H_{14}O_4$ (174), a species that was observed in the aqueous PA experiments (Scheme 3). In summary, there is significant overlap in the products of gas-phase photolysis of PAMe and aqueous-phase photolysis of PA suggesting that the mechanism of photolysis is not drastically different in the two phases.

C. Theoretically Predicted Photolysis Pathways. The calculated minimal energy structure of PA, PAMe−H_2O complex, and PAMe−$(H_2O)_5$ cluster calculated at the MP2/cc-PVDZ level of theory are presented in Figure S13 of the Supporting Information. Tables S4 and S5 in the Supporting Information compare the electronic singlet-state energies calculated at the ADC(2) and OM2/MRCI levels for bare PA. The positions of the first (4.2 and 4.0 eV in ADC(2) and OM2/MRCI, respectively) and second (5.9 and 5.2 eV, respectively) singlet electronic states, S_1 and S_2, are similar in both methods relative to the ground state. The agreement becomes worse for higher electronic states; however, they are not expected to play an active role in the photodissociation dynamics. Furthermore, S_2 is centered on the carboxylic acid group of the molecule, which should not participate in photochemistry at the tropospherically relevant excitation wavelengths. Therefore, the simulations of photodissociation dynamics in both PA and PAMe included only the S_1 state, which is centered on the carbonyl group.

The lowest triplet state (T_1) in the ADC(2) method lies about 0.2 eV above S_1. With the OM2/MRCI method, T_1 lies about 0.3 eV below S_1. In both cases, the energy gap between the first and the second triplet states, T_1 and T_2, is about 2 eV. As explained in the Computational Methods, the MD simulations on the T_1 state were initiated by enforcing an ISC transition to the T_1 surface at the location of the smallest S_1-T_1 energy gap.

The MD simulations on the T_1 surface were confined to 10 ps in the initial runs. The fraction of the trajectories leading to a photochemical reaction in the 10 ps time window was 32%. However, we found that this fraction increased to 69% when the simulation times were increased to 100 ps. Despite the increased computational costs, all the subsequent trajectories were propagated for 100 ps to more faithfully represent the dynamics. A comparison of 10 and 100 ps trajectories for bare PA is given in Table S6 in the Supporting Information.

All the reactive and nonreactive events observed in the 100 ps simulations of PA, PAMe−H_2O, and PAMe−$(H_2O)_5$, and the number of trajectories that produced these events are summarized in Table 3. Figures S14−S20 in the Supporting

**Table 3. Comparison of the MD-Simulated Reaction Yields in the PA, PAMe−H_2O, and PAMe−$(H_2O)_5$ Systems[a]**

events	PA 300 K	PAMe− H_2O 300 K	PAMe− $(H_2O)_5$ 200 K	PAMe− $(H_2O)_5$ 300 K
no reaction/water evaporation	31	68	52	39
Norrish type II (H transfer)	10	2	5	3
Norrish type I (loss of $CH_3C(O)^\bullet$)	37	18	8	24
ring opening	10	5	18	18
loss of $^\bullet C(O)OH$ (decarboxylation) or loss of $^\bullet C(O)OCH_3$	12	6	17	16

[a]The table lists the number of trajectories resulting in a particular product channel. The total number of trajectories is 100 in all cases except for PAMe−H_2O, where the total is 99 because one of the trajectories crashed.

Information present the histograms of the number of trajectories that occur in a particular time bin, and histograms

of the number of water molecules still remaining in PAMe−$(H_2O)_5$ at the time of the reaction. Figure 6 shows selected snapshots corresponding to the different reaction pathways observed in the bare PA calculations. The following types of events were observed in the simulations of PA and PAMe/water. (1) No reaction and/or water evaporation was the most common outcome in all cases, even after 100 ps of simulation. (2) An H-atom transfer from the methyl group to the carbonyl group (Figure 6a), the initial step in the Norrish type II reaction, occurred in some of the trajectories. There was no clear preference for early vs late timing of this event in the 0−100 ps window. It is conceivable that the probability of this reaction could further increase for longer trajectories but we have not investigated this possibility in view of the computational costs. (3) The loss of the $CH_3C(O)^\bullet$ radical corresponding to the Norrish type I reaction was the most frequently observed reaction pathway. Its occurrence also was distributed throughout the entire 100 ps simulation window. (4) A significant number of trajectories culminated in an opening of the cyclobutyl ring (Figure 6b). In all systems, it either occurred on an ultrafast time scale in less than 20 fs or did not occur at all. (5) Decarboxylation, i.e., the loss of $^\bullet C(O)OH$ from PA, as shown in Figure 6c, or the corresponding loss of $^\bullet C(O)OCH_3$ from PAMe, was observed in some of the trajectories. In all cases it was ultrafast, occurring within 500 fs. This is the only process that has no analog with the experimentally observed reactions.

The computational results describing the photochemical reactions support the experimental results reasonably well. The effect of the water molecule(s) on the distribution of different pathways was not dramatic, in good qualitative agreement with the experimental observation of the lack of suppression of photolysis of PA in an aqueous solution. The cyclobutyl ring-opening, Norrish-I, Norrish-II, and the hydrogen transfer were observed in both the experimental and computational approach. The prediction of the decarboxylation event, which was not observed in the experiments, is an interesting result that definitively merits further study. The decarboxylation pathways were unexpected because the carboxyl group is sufficiently isolated from the carbonyl group, which initially accepts the excitation. However, molecular orbitals of PA shown in the Supporting Information Figures S21 and S22,

t = 59.08 ps

t = 59.18 ps

a)

t = 0 fs   t = 100 fs

b)

c)
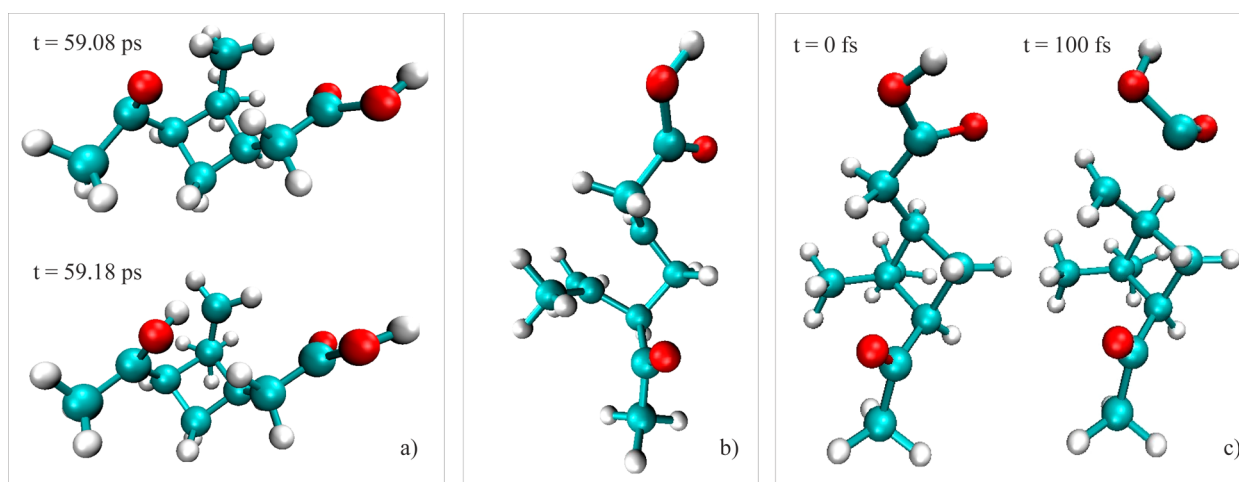
Figure 6. Representative snapshots of MD trajectories taken shortly after the following reactions took place: (a) H-transfer to CO group; (b) opening of the four-membered ring; (c) decarboxylation.

suggest that the T_1 state of PA does have some molecular orbital density on the carboxyl end of the molecule (the S_1 state is localized on the carbonyl end, as expected). Following the theoretical predictions, we re-examined the experimental data for the evidence of this pathway but could not conclusively identify it. It is plausible that some decarboxylation products were formed but were not detected in this study due to experimental limitations (such as lack of sensitivity to decarboxylated products in the ESI-MS measurements or evaporative loss of these products, especially smaller molecular weight products, during the derivatization for GC−CIMS). It is also possible that our assumption that only the T_1 state contributes to the photodissociation dynamics is incorrect, and photolysis proceeds on S_1 on long ($\gg$10 ps) time scales without any decarboxylation; however, our computational tools are insufficient to fully test this assumption.

D. Conclusions and Atmospheric Implications. In this work, aqueous photochemistry of PA as a representative product of BVOC oxidation was investigated. The photolysis rate, quantum yield, photolysis products, and chemical mechanisms were determined using several methods. Specifically, UV−vis spectroscopy provided information about the kinetics of the aqueous PA photolysis, as the disappearance of the characteristic $\pi^* \leftarrow$ n carbonyl band at 280 nm was followed as a function of time. Chemical actinometry was used to quantify the spectral flux density and allowed the determination of the photolysis quantum yield. GC−CIMS and LC−ESI-MS were used to survey the products formed in the aqueous photolysis of PA and determine their formulas based on the accurate masses in the mass spectra. Selected photolyzed products were separated using semipreparative HPLC, and further analyzed by ^{1}H and ^{13}C NMR, which provided structural information and allowed us to confirm our assignment of the main product of photolysis. Gas-phase photolysis of PAMe was carried out for comparison with the aqueous photolysis, and the photolysis process was followed in real time with a PTR-ToF-MS instrument. Finally, computational methods were used to explore the excited-state dynamics and provided useful information about the photolysis process, supporting the experimental findings. This combination of methods was necessary for the comprehensive characterization of the PA photolysis mechanism.

We found that the dominant photolysis pathway is a conversion of PA into its structural isomer, limononic acid. This product cannot be used as a unique tracer of PA photolysis because it is readily produced by ozonolysis of *d*-limonene,[91] another common monoterpene. This example highlights the difficulties in attributing specific tracers to specific precursors. It is possible that in areas dominated by α-pinene, the formation of the limononic acid through PA photolysis could be misinterpreted as a result of d-limonene oxidation.

The quantum yield (∼0.5) for the aqueous PA photolysis (which is dominated by isomerization) is quite large, considering that molecules in solutions generally tend to resist photochemistry. The gas-phase photolysis yield of PAMe is similarly large, with a lower limit of 0.53. This gas-phase quantum yield could potentially be as high as unity because our gas-phase measurements can only detect processes that result in fragmentation of PA; we cannot observe isomerization as we do in the aqueous phase. The lack of significant photolysis suppression by the solvent is consistent with intramolecular isomerization as the primary photolysis step. Indeed, the

structure of PA is near-optimal for the H-atom transfer from the $-CH_3$ group to the excited carbonyl group, facilitating the Norrish-II process. We note that the presence of water molecules in PA/water clusters did not have a significant effect on the calculated time scales of photolysis or distribution of products.

One of the goals of this study was to provide insight into the relevance of the direct aqueous photolysis of organic compounds found in SOA compared to OH-mediated photochemical aging, using PA as a prototypical example. To put our measurements in perspective, we compare rates of direct aqueous photolysis to the rate of removal due to gaseous photolysis, gaseous oxidation by OH radical, and aqueous oxidation by OH radical on the basis of the methods outlined by Epstein et al.[92,93] We assume that PA partitions into cloud and fog droplets according to Henry's law. Measurements of the Henry's law constant of PA are not available; therefore, we employ HENRYWIN v3.20[5] developed by the Environmental Protection Agency to predict the effective Henry's law constant of PA. The fraction of PA dissolved in a cloud also depends on the cloud liquid water content (LWC). LWC is highly variable throughout the atmosphere, but we use a value of 0.5 g m^{-3}, generally the largest value routinely found in the atmosphere,[94,95] to determine the maximum contribution of aqueous removal processes. The rate constant for oxidation by OH in the aqueous and gaseous phase were predicted with structure activity relationships developed by Monod and Doussin[96,97] and Kwok and Atkinson,[98] respectively. We employed the NCAR Tropospheric Ultraviolet & Visible Radiation Model (Edition 4.4)[99] to predict the actinic flux as a function of solar zenith angle (SZA) at the globally averaged surface albedo of 0.154.[100] Our experimentally determined aqueous extinction coefficients (Table 1 in the Supporting Information) were used to calculate the rates of aqueous photolysis. Gas-phase absorption cross sections of PA were not available in the literature. Therefore, we used the absorption cross sections of acetone as a substitute.[48] Gas-phase OH radical concentrations were correlated to the rate of O^{1}D photolysis according to Rohrer and Berresheim.[101] We used aqueous OH radical daytime and nighttime concentrations of 10^{-13} and 10^{-14} M, respectively.[18] Because the exact dependence of aqueous OH radical concentrations on SZA is unknown, we varied concentrations according to the same dependence of the gas-phase OH radical concentrations on SZA.

Figure 7a details the selectivity of each chemical removal pathway as a function of SZA. In a wet air mass with a LWC of 0.5 g m^{-3}, atmospheric removal of PA is dominated by aqueous oxidation by OH radical. Aqueous photolysis is the second-most competitive chemical sink, but it is only responsible for removing less than 2% of PA. Photolysis rates are more strongly dependent on SZA than rates of oxidation by the OH radical, but selectivity is largely independent of SZA from 0 to 60°. In the absence of liquid water at solar zenith angles less than 70°, gaseous photolysis would be responsible for removal of approximately 40% of the total PA mass, with the rest consumed by the gas-phase OH oxidation. We conclude that aqueous photolysis of PA will only be important in cloud and fog droplets under conditions of significantly depleted OH radical concentrations.

We also investigated the chemical removal of PA in the presence of a wet aerosol. In this scenario, we assume a total organic aerosol mass concentration of 20 μg m^{-3}, typical of moderately polluted urban conditions, with the particles
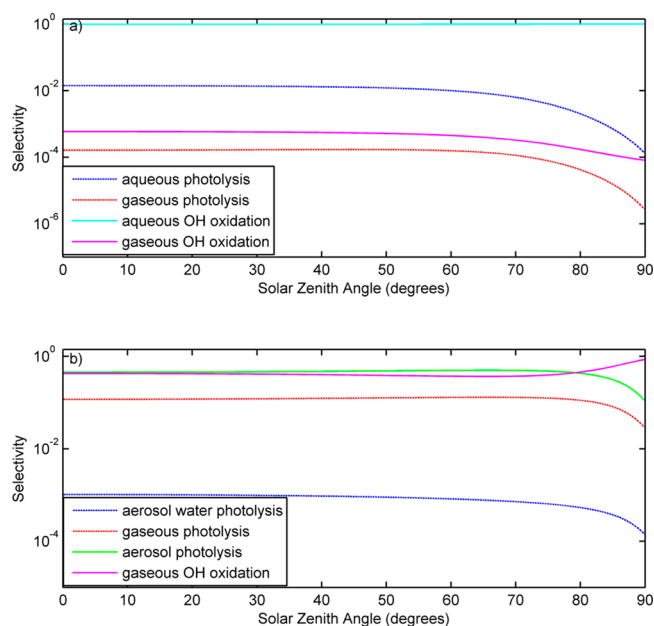
Figure 7. (a) Calculated PA removal selectivity of key chemical processes likely to affect PA in the presence of cloud and fog droplets. The selectivity of aqueous photolysis, gaseous photolysis, aqueous oxidation by OH radical, and gaseous oxidation by OH radical are plotted as a function of solar zenith angle. LWC = 0.5 g m^{-3} and T = 298 K. (b) Calculated PA removal selectivity of key chemical processes likely to affect PA in a polluted atmosphere without cloud or fog droplets. The selectivity of photolysis in aerosol water, photolysis in the gas phase, photolysis in the organic-aerosol phase, and oxidation by OH radical in the gas phase are compared. (The total organic aerosol concentration is 20 μg m^{-3}, liquid water concentration in particles is 50 μg m^{-3}, and T = 298 K.)

carrying 50 μg m^{-3} of water. The gas phase to organic-aerosol phase partitioning of PA is modeled with a standard absorptive partitioning approach.[102,103] The equilibrium vapor pressure of PA (C^* = 5.2 μg/m^3), obtained from measurements,[6] leads to partitioning behavior roughly consistent with field studies in ref 104. The partitioning between the gas phase and aqueous-aerosol phase is approximated with Henry's law (even though the solubility of PA in solute-rich aerosol water may be quite different from that in a dilute solution). Henry's law may not apply under specific atmospheric conditions.[65] However, without considering specific conditions that would likely be experienced on a local scale, Henry's law provides a reasonable overall estimate of gas/aqueous partitioning.[94] For simplicity, we assume that the aqueous and organic aerosol phases do not directly communicate with each other and that OH radical is depleted inside particles to the point that it does not participate in chemistry (the validity of this assumption is hard to test in view of the highly uncertain free radical concentrations inside particles). The measured PA aqueous photolysis parameters are used to calculate the PA photolysis rates in the aqueous-aerosol phase; for the organic-aerosol phase, the photophysical parameters of PA are assumed to be the same as for gas-phase acetone. Figure 7b shows the selectivity of the following chemical removal pathways as a function of SZA: photolysis in the aqueous-aerosol phase, photolysis in the organic-aerosol phase, gaseous photolysis, and gaseous oxidation by OH. Both aerosol photolysis and gaseous oxidation by OH are competitive and are responsible for removal of roughly 88% of the total PA mass at solar zenith angles less than 60°. The

contribution of photolysis in the aqueous-aerosol phase is rather insignificant due to the low LWC in particles (several orders of magnitude lower than in a typical cloud).

Even though aqueous photolysis is not a major loss mechanism for PA under realistic atmospheric conditions, the finding that the photolysis quantum yield is not significantly reduced by the presence of a condensed phase is important in the context of SOA aging. The prevailing view is that most of the SOA photo-oxidation chemistry is confined to the gas phase, whereas molecules partitioned in the organic-aerosol phase are shielded from photochemical processing.[105] This assumption likely holds with respect to processing by OH oxidation.[106] However, if the molecule has photolabile functional groups, hiding inside an aerosol particle may not protect it from loss because of the large penetration depth for actinic radiation inside particles. A number of SOA compounds are both considerably more water-soluble and also considerably less volatile than PA. These more oxidized products will have a stronger preference for the condensed phase (organic or aqueous) than PA, with the corresponding increase in the relative importance of condensed-phase photolysis over gas-phase oxidation.

■ ASSOCIATED CONTENT

Ⓢ Supporting Information

List of abbreviations used in the paper; details of aqueous photolysis experiments; absorption cross sections and molar extinction coefficients of aqueous PA; description of the actinometer used in aqueous photolysis measurements; analysis of broadband-UV aqueous photolysis data; description of HPLC separation of PA photolysis products and fraction collection; details of gas-phase photolysis experiments and data analysis; derivation of equations for the three kinetics models of aqueous-phase photolysis of PA; and a computational section including minimum energy structures of studied species, details and comparisons of dynamics simulations, description and comparison of the observed events at different temperatures, and histograms of time distributions for different reaction pathways. This information is available free of charge via the Internet at http://pubs.acs.org.

■ AUTHOR INFORMATION

Corresponding Author

*S. Nizkorodov: e-mail, nizkorod@uci.edu; phone, 1-949-824-1262.

Notes

The authors declare no competing financial interest.

■ ACKNOWLEDGMENTS

■ REFERENCES

(1) Finlayson-Pitts, B. J.; Pitts, J. N., Jr. *Chemistry of the Upper and Lower Atmosphere: Theory, Experiments and Applications*; Academic Press: San Diego, CA, 2000.

(2) Kanakidou, M.; Seinfeld, J. H.; Pandis, S. N.; Barnes, I.; Dentener, F. J.; Facchini, M. C.; Van Dingenen, R.; Ervens, B.; Nenes, A.; Nielsen, C. J.; et al. Organic Aerosol and Global Climate Modelling: A Review. *Atmos. Chem. Phys.* **2005**, *5*, 1053−1123.

(3) Guenther, A. B.; Jiang, X.; Heald, C. L.; Sakulyanontvittaya, T.; Duhl, T.; Emmons, L. K.; Wang, X. The Model of Emissions of Gases and Aerosols from Nature Version 2.1 (MEGAN2.1): An Extended and Updated Framework for Modeling Biogenic Emissions. *Geosci. Model Dev.* **2012**, *5*, 1471−1492.

(4) Yasmeen, F.; Vermeylen, R.; Maurin, N.; Perraudin, E.; Doussin, J.-F.; Claeys, M. Characterisation of Tracers for Aging of a-Pinene Secondary Organic Aerosol Using Liquid Chromatography/Negative Ion Electrospray Ionisation Mass Spectrometry. *Environ. Chem.* **2012**, *9*, 236−246.

(5) U.S. Environmental Protection Agency, E. EPA HENRYWIN V3.20, 2011.

(6) Bilde, M.; Pandis, S. N. Evaporation Rates and Vapor Pressures of Individual Aerosol Species Formed in the Atmospheric Oxidation of α- and β-Pinene. *Environ. Sci. Technol.* **2001**, *35*, 3344−3349.

(7) Yu, J.; Flagan, R. C.; Seinfeld, J. H. Identification of Products Containing -COOH, -OH, and -C=O in Atmospheric Oxidation of Hydrocarbons. *Environ. Sci. Technol.* **1998**, *32*, 2357−2370.

(8) Yu, J.; Cocker, D. R. I.; Griffin, R. J.; Flagan, R. C.; Seinfeld, J. H. Gas-Phase Ozone Oxidation of Monoterpenes: Gaseous and Particulate Products. *J. Atmos. Chem.* **1999**, *34*, 207−258.

(9) Yu, J.; Griffin, R. J.; Cocker, D. R. I.; Flagan, R. C.; Seinfeld, J. H.; Blanchard, P. Observation of Gaseous and Particulate Products of Monoterpene Oxidation in Forest Atmospheres. *Geophys. Res. Lett.* **1999**, *26*, 1145−1148.

(10) Jaoui, M.; Kamens, R. M. Gas Phase Photolysis of Pinonaldehyde in the Presence of Sunlight. *Atmos. Environ.* **2003**, *37*, 1835−1851.

(11) Müller, L.; Reinnig, M.-C.; Naumann, K. H.; Saathoff, H.; Mentel, T. F.; Donahue, N. M.; Hoffmann, T. Formation of 3-Methyl-1,2,3-Butanetricarboxylic Acid Via Gas Phase Oxidation of Pinonic Acid − a Mass Spectrometric Study of SOA Aging. *Atmos. Chem. Phys.* **2012**, *12*, 1483−1496.

(12) Cheng, Y.; Li, S.-M.; Leithead, A.; Brickell, P. C.; Leaitch, W. R. Characterizations of Cis-Pinonic Acid and n-Fatty Acids on Fine Aerosols in the Lower Fraser Valley During Pacific 2001 Air Quality Study. *Atmos. Environ.* **2004**, *38*, 5789−5800.

(13) Cheng, Y.; Li, S.-M. Nonderivatization Analytical Method of Fatty Acids and Cis-Pinonic Acid and Its Application in Ambient PM2.5 Aerosols in the Greater Vancouver Area in Canada. *Environ. Sci. Technol.* **2005**, *39*, 2239−2246.

(14) Raja, S.; Raghunathan, R.; Yu, X.-Y.; Lee, T.; Chen, J.; Kommalapati, R. R.; Murugesan, K.; Shen, X.; Qingzhong, Y.; Valsaraj, K. T.; et al. Fog Chemistry in the Texas−Louisiana Gulf Coast Corridor. *Atmos. Environ.* **2008**, *42*, 2048−2061.

(15) O'Dowd, C. D.; Aalto, P.; Hämeri, K.; Kulmala, M.; Hoffmann, T. Aerosol Formation: Atmospheric Particles from Organic Vapours. *Nature* **2002**, *416*, 497−498.

(16) Hyvärinen, A.-P.; Lihavainen, H.; Gaman, A.; Vairila, L.; Ojala, H.; Kulmala, M.; Viisanen, Y. Surface Tensions and Densities of Oxalic, Malonic, Succinic, Maleic, Malic, and Cis-Pinonic Acids. *J. Chem. Eng. Data* **2005**, *51*, 255−260.

(17) Li, X.; Hede, T.; Tu, Y.; Leck, C.; Ågren, H. Surface-Active Cis-Pinonic Acid in Atmospheric Droplets: A Molecular Dynamics Study. *J. Phys. Chem. Lett.* **2010**, *1*, 769−773.

(18) Ervens, B.; Turpin, B. J.; Weber, R. J. Secondary Organic Aerosol Formation in Cloud Droplets and Aqueous Particles (AqSOA): A Review of Laboratory, Field and Model Studies. *Atmos. Chem. Phys.* **2011**, *11*, 11069−11102.

(19) McNeill, V. F.; Grannas, A. M.; Abbatt, J. P. D.; Ammann, M.; Ariya, P.; Bartels-Rausch, T.; Domine, F.; Donaldson, D. J.; Guzman, M. I.; Heger, D.; et al. Organics in Environmental Ices: Sources, Chemistry, and Impacts. *Atmos. Chem. Phys.* **2012**, *12*, 9653−9678.

(20) Faust, B. C.; Anastasio, C.; Allen, J. M.; Arakaki, T. Aqueous-Phase Photochemical Formation of Peroxides in Authentic Cloud and Fog Waters. *Science* **1993**, *260*, 73−75.

(21) Vaida, V. Perspective: Water Cluster Mediated Atmospheric Chemistry. *J. Chem. Phys.* **2011**, *135*, 020901−8.

(22) Meng, Z. Y.; Seinfeld, J. H.; Saxena, P.; Kim, Y. P. Contribution of Water to Particulate Mass in the South Coast Air Basin. *Aerosol Sci. Technol.* **1995**, *22*, 111−123.

(23) Wang, J.; Jacob, D. J.; Martin, S. T. Effect of the Hysteresis of Particle Phase Transitions. *J. Geophys. Res.* **2008**, *113*, D11206 DOI: 10.1029/2007JD009367.

(24) Blando, J. D.; Turpin, B. J. Secondary Organic Aerosol Formation in Cloud and Fog Droplets: A Literature Evaluation of Plausibility. *Atmos. Environ.* **2000**, *34*, 1623−1632.

(25) Jang, M.; Czoschke, N. M.; Lee, S.; Kamens, R. M. Heterogeneous Atmospheric Aerosol Production by Acid-Catalyzed Particle-Phase Reactions. *Science* **2002**, *298*, 814−817.

(26) Lee, A. K. Y.; Zhao, R.; Gao, S. S.; Abbatt, J. P. D. Aqueous-Phase OH Oxidation of Glyoxal: Application of a Novel Analytical Approach Employing Aerosol Mass Spectrometry and Complementary Off-Line Techniques. *J. Phys. Chem. A* **2011**, *115*, 10517−10526.

(27) Lee, A. K. Y.; Herckes, P.; Leaitch, W. R.; Macdonald, A. M.; Abbatt, J. P. D. Aqueous OH Oxidation of Ambient Organic Aerosol and Cloud Water Organics: Formation of Highly Oxidized Products. *Geophys. Res. Lett.* **2011**, *38*, L11805 DOI: 10.1029/2011GL047439.

(28) Lee, A. K. Y.; Hayden, K. L.; Herckes, P.; Leaitch, W. R.; Liggio, J.; Macdonald, A. M.; Abbatt, J. P. D. Characterization of Aerosol and Cloud Water at a Mountain Site During WACS 2010: Secondary Organic Aerosol Formation through Oxidative Cloud Processing. *Atmos. Chem. Phys.* **2012**, *12*, 7103−7116.

(29) Liu, Y.; Siekmann, F.; Renard, P.; El Zein, A.; Salque, G.; El Haddad, I.; Temime-Roussel, B.; Voisin, D.; Thissen, R.; Monod, A. Oligomer and Soa Formation through Aqueous Phase Photooxidation of Methacrolein and Methyl Vinyl Ketone. *Atmos. Environ.* **2012**, *49*, 123−129.

(30) Nguyen, T. B.; Coggon, M. M.; Flagan, R. C.; Seinfeld, J. H. Reactive Uptake and Photo-Fenton Oxidation of Glycolaldehyde in Aerosol Liquid Water. *Environ. Sci. Technol.* **2013**, *47*, 4307−4316.

(31) Ervens, B.; Wang, Y.; Eagar, J.; Leaitch, W. R.; Macdonald, A. M.; Valsaraj, K. T.; Herckes, P. Dissolved Organic Carbon (DOC) and Select Aldehydes in Cloud and Fog Water: The Role of the Aqueous Phase in Impacting Trace Gas Budgets. *Atmos. Chem. Phys.* **2013**, *13*, 5117−5135.

(32) Chen, J.; Griffin, R. J.; Grini, A.; Tulet, P. Modeling Secondary Organic Aerosol Formation through Cloud Processing of Organic Compounds. *Atmos. Chem. Phys.* **2007**, *7*, 5343−5355.

(33) Carlton, A. G.; Turpin, B. J.; Lim, H.-J.; Altieri, K. E.; Seitzinger, S. P. Link between Isoprene and Secondary Organic Aerosol (SOA): Pyruvic Acid Oxidation Yields Low Volatility Organic Acids in Clouds. *Geophys. Res. Lett.* **2006**, *33*, L06822 (1−4) DOI: 10.1029/2005GL025374.

(34) Carlton, A. G.; Turpin, B. J.; Altieri, K. E.; Seitzinger, S. P.; Mathur, R.; Roselle, S. J.; Weber, R. J. Cmaq Model Performance Enhanced When in-Cloud Secondary Organic Aerosol Is Included: Comparisons of Organic Carbon Predictions with Measurements. *Environ. Sci. Technol.* **2008**, *42*, 8798−8802.

(35) Fu, T.-M.; Jacob, D. J.; Wittrock, F.; Burrows, J. P.; Vrekoussis, M.; Henze, D. K. Global Budgets of Atmospheric Glyoxal and Methylglyoxal, and Implications for Formation of Secondary Organic Aerosols. *J. Geophys. Res.* **2008**, *113*, D15303 DOI: 10.1029/2007JD009505.

(36) Dzepina, K.; Volkamer, R. M.; Madronich, S.; Tulet, P.; Ulbrich, I. M.; Zhang, Q.; Cappa, C. D.; Ziemann, P. J.; Jimenez, J. L. Evaluation of Recently-Proposed Secondary Organic Aerosol Models for a Case Study in Mexico City. *Atmos. Chem. Phys.* **2009**, *9*, 5681−5709.

12943

dx.doi.org/10.1021/jp4093018 | *J. Phys. Chem. A* 2013, 117, 12930−12945

(37) Ervens, B.; Volkamer, R. M. Glyoxal Processing by Aerosol Multiphase Chemistry: Towards a Kinetic Modeling Framework of Secondary Organic Aerosol Formation in Aqueous Particles. *Atmos. Chem. Phys* **2012**, *10*, 8219−8244.

(38) Baldwin, P. J.; Canosa-Mas, C. E.; Frey, H. M.; Walsh, R. The Photochemistry of Cyclobutyl Methyl Ketone. Part 1. Room-Temperature Results and the General Mechanism. *J. Chem. Soc., Faraday Trans.* **1987**, *83*, 1049−58.

(39) Baldwin, P. J.; Canosa-Mas, C. E.; Frey, H. M.; Walsh, R. The Photochemistry of Methyl Cyclobutyl Ketone. Part 2. Temperature Dependence and the Acetyl Radical Decomposition. *Int. J. Chem. Kinet* **1987**, *19*, 997−1013.

(40) Norman, I.; Pitts, J. N., Jr. Structure and Reactivity in the Vapor-Phase Photolysis of Ketones. III. Methyl Cyclobutyl Ketone. *J. Am. Chem. Soc.* **1955**, *77*, 6104−6107.

(41) Praplan, A. P.; Barmet, P.; Dommen, J.; Baltensperger, U. Cyclobutyl Methyl Ketone as a Model Compound for Pinonic Acid to Elucidate Oxidation Mechanisms. *Atmos. Chem. Phys. Discuss.* **2012**, *12*, 10651−10678.

(42) Shaffer, G. W.; Doerr, A. B.; Purzycki, K. L. Photoisomerization of Nopinone. *J. Org. Chem.* **1972**, *37*, 25−29.

(43) Nozière, B.; Barnes, I.; Becker, K.-H. Product Study and Mechanisms of the Reactions of α-Pinene and of Pinonaldehyde with OH Radicals. *J. Geophys. Res.* **1999**, *104*, 23645−23656.

(44) Leermakers, P. A.; Vesley, G. F. The Photochemistry of A-Keto Acids and A-Keto Esters. I. Photolysis of Pyruvic Acid and Benzoylformic Acid. *J. Am. Chem. Soc.* **1963**, *85*, 3776−3779.

(45) Guzmán, M. I.; Colussi, A. J.; Hoffmann, M. R. Photoinduced Oligomerization of Aqueous Pyruvic Acid. *J. Phys. Chem. A* **2006**, *110*, 3619−3626.

(46) Griffith, E. C.; Carpenter, B. K.; Shoemaker, R. K.; Vaida, V. Photochemistry of Aqueous Pyruvic Acid. *Proc. Natl. Acad. Sci.* **2013**, *110*, 11714−11719.

(47) Bunce, N. J.; Lamarre, J.; Vaish, S. P. Photorearrangement of Azoxybenzene to 2-Hydroxyazobenzene: A Convenient Chemical Actinometer. *Photochem. Photobiol.* **1984**, *39*, 531−533.

(48) Sander, S. P.; Abbatt, J.; Barker, J. R.; Burkholder, J. B.; Friedl, R. R.; Golden, D. M.; Huie, R. E.; Kolb, C. E.; Kurylo, M. J.; Moortgat, G. K.; et al. *Chemical Kinetics and Photochemical Data for Use in Atmospheric Studies*; Evaluation No. 17; JPL Publication Jet Propulsion Laboratory: Pasadena, CA, 2011; Publication 10-6.

(49) Xie, H.-b.; Jin, L.; Rudić, S.; Simons, J. P.; Gerber, R. B. Computational Studies of Protonated β-D-Galactose and Its Hydrated Complex: Structures, Interactions, Proton Transfer Dynamics, and Spectroscopy. *J. Phys. Chem. B* **2012**, *116*, 4851−4859.

(50) Xie, H.-B.; Gerber, R. B. Interaction and Reaction of the Hydroxyl Ion with β-D-Galactose and Its Hydrated Complex: An Ab Initio Molecular Dynamics Study. *Phys. Chem. Chem. Phys.* **2012**, *14*, 12086−12089.

(51) Shemesh, D.; Gerber, R. B. Femtosecond Timescale Deactivation of Electronically Excited Peroxides at Ice Surfaces. *Mol. Phys.* **2012**, *110*, 605−617.

(52) Miller, Y.; Finlayson-Pitts, B. J.; Gerber, R. B. Ionization of N_2O_4 in Contact with Water: Mechanism, Time Scales and Atmospheric Implications. *J. Am. Chem. Soc.* **2009**, *131*, 12180−12185.

(53) Raff, J. D.; Njegic, B.; Chang, W. L.; Gordon, M. S.; Dabdub, D.; Gerber, R. B.; Finlayson-Pitts, B. J. Chlorine Activation Indoors and Outdoors Via Surface-Mediated Reactions of Nitrogen Oxides with Hydrogen Chloride. *Proc. Natl. Acad. Sci.* **2009**, *106*, 13647−13654.

(54) Buszek, R. J.; Torrent-Sucarrat, M.; Anglada, J. M.; Francisco, J. S. Effects of a Single Water Molecule on the OH + H_2O_2 Reaction. *J. Phys. Chem. A* **2012**, *116*, 5821−5829.

(55) Buszek, R. J.; Barker, J. R.; Francisco, J. S. Water Effect on the OH + HCl Reaction. *J. Phys. Chem. A* **2012**, *116*, 4712−4719.

(56) Gonzalez, J.; Anglada, J. M.; Buszek, R. J.; Francisco, J. S. Impact of Water on the OH + HOCl Reaction. *J. Am. Chem. Soc.* **2011**, *133*, 3345−3353.

(57) de Jesus Medeiros, D.; Pimentel, A. S. New Insights in the Atmospheric Hono Formation: New Pathways for N_2O Isomerization

and NO_2 Dimerization in the Presence of Water. *J. Phys. Chem. A* **2011**, *115*, 6357−6365.

(58) Scaldaferri, M. C. L.; Pimentel, A. S. Born−Oppenheimer Molecular Dynamics on the H_2S + NO_3 Reaction in the Presence and Absence of Water: The Kinetic Isotope Effect. *J. Phys. Chem. A* **2010**, *114*, 8993−8998.

(59) Weber, W.; Thiel, W. Orthogonalization Corrections for Semiempirical Methods. *Theor. Chem. Acc.* **2000**, *103*, 495−506.

(60) Dunning, T. H. Gaussian-Basis Sets for Use in Correlated Molecular Calculations 0.1. The Atoms Boron through Neon and Hydrogen. *J. Chem. Phys.* **1989**, *90*, 1007−1023.

(61) Weigend, F.; Haser, M. RI-MP2: First Derivatives and Global Consistency. *Theor. Chem. Acc.* **1997**, *97*, 331−340.

(62) Ahlrichs, R.; Bar, M.; Haser, M.; Horn, H.; Kolmel, C. Electronic-Structure Calculations on Workstation Computers - the Program System Turbomole. *Chem. Phys. Lett.* **1989**, *162*, 165−169.

(63) Schirmer, J. Beyond the Random-Phase Approximation - a New Approximation Scheme for the Polarization Propagator. *Phys. Rev. A* **1982**, *26*, 2395−2416.

(64) Koslowski, A.; Beck, M. E.; Thiel, W. Implementation of a General Multireference Configuration Interaction Procedure with Analytic Gradients in a Semiempirical Context Using the Graphical Unitary Group Approach. *J. Comput. Chem.* **2003**, *24*, 714−726.

(65) Epstein, S. A.; Shemesh, D.; Tran, V. T.; Nizkorodov, S. A.; Gerber, R. B. Absorption Spectra and Photolysis of Methyl Peroxide in Liquid and Frozen Water. *J. Phys. Chem. A* **2012**, *116*, 6068−6077.

(66) Shemesh, D.; Lan, Z. G.; Gerber, R. B. Dynamics of Triplet-State Photochemistry of Pentanal: Mechanisms of Norrish I, Norrish II and H Abstraction Reactions. *J. Phys. Chem. A* **2013**, *117*, 11711−11724.

(67) Shemesh, D.; Gerber, R. B. Classical Trajectory Simulations of Photoionization Dynamics of Tryptophan: Intramolecular Energy Flow, Hydrogen-Transfer Processes and Conformational Transitions. *J. Phys. Chem. A* **2006**, *110*, 8401−8408.

(68) Shemesh, D.; Gerber, R. B. Different Chemical Dynamics for Different Conformers of Biological Molecules: Photoionization of Glycine. *J. Chem. Phys.* **2005**, *122*, 241104 (1−4).

(69) Shemesh, D.; Baer, R.; Seideman, T.; Gerber, R. B. Photoionization Dynamics of Glycine Adsorbed on a Silicon Cluster: "On-the-Fly" Simulations. *J. Chem. Phys.* **2005**, *122*, 184704 (1−9).

(70) Shemesh, D.; Chaban, G. M.; Gerber, R. B. Photoionization Dynamics of Glycine: The First 10 Picoseconds. *J. Phys. Chem. A* **2004**, *108*, 11477−11484.

(71) Miller, Y.; Chaban, G. M.; Finlayson-Pitts, B. J.; Gerber, R. B. Photochemical Processes Induced by Vibrational Overtone Excitations: Dynamics Simulations for Cis-HONO, Trans-HONO, HNO_3, and HNO_3-H_2O. *J. Phys. Chem. A* **2006**, *110*, 5342−5354.

(72) Miller, Y.; Gerber, R. B. Dynamics of Vibrational Overtone Excitations of H_2SO_4, H_2SO_4-H_2O: Hydrogen-Hopping and Photodissociation Processes. *J. Am. Chem. Soc.* **2006**, *128*, 9594−9595.

(73) Thiel, W. *MNDO Program*, Version 6.1; Mülheim an Der Ruhr, Germany, 2007.

(74) Fabiano, E.; Keal, T. W.; Thiel, W. Implementation of Surface Hopping Molecular Dynamics Using Semiempirical Methods. *Chem. Phys.* **2008**, *349*, 334−347.

(75) Turro, N. J.; Scaiano, J. C.; Ramamurthy, V. *Modern Molecular Photochemistry of Organic Molecules*; University Science Books: Mill Valley, CA, 2010.

(76) Bernard, Y. A.; Shao, Y. H.; Krylov, A. I. General Formulation of Spin-Flip Time-Dependent Density Functional Theory Using Non-Collinear Kernels: Theory, Implementation, and Benchmarks. *J. Chem. Phys.* **2012**, *136* (204103), 1−17.

(77) Etinski, M.; Fleig, T.; Marian, C. A. Intersystem Crossing and Characterization of Dark States in the Pyrimidine Nucleobases Uracil, Thymine, and 1-Methylthymine. *J. Phys. Chem. A* **2009**, *113*, 11809−11816.

(78) Marian, C. M. Spin-Orbit Coupling and Intersystem Crossing in Molecules. *Wiley Interdiscip. Rev.: Comput. Mol. Sci.* **2012**, *2*, 187−203.

(79) Richter, M.; Marquetand, P.; Gonzalez-Vazquez, J.; Sola, I.; Gonzalez, L. Sharc: Ab Initio Molecular Dynamics with Surface Hopping in the Adiabatic Representation Including Arbitrary Couplings. *J. Chem. Theory. Comput.* **2011**, *7*, 1253−1258.

(80) Marquetand, P.; Richter, M.; Gonzalez-Vazquez, J.; Sola, I.; Gonzalez, L. Nonadiabatic Ab Initio Molecular Dynamics Including Spin-Orbit Coupling and Laser Fields. *Faraday Discuss.* **2011**, *153*, 261−273.

(81) Tully, J. C. Molecular-Dynamics with Electronic-Transitions. *J. Chem. Phys.* **1990**, *93*, 1061−1071.

(82) Sellner, B.; Barbatti, M.; Lischka, H. Dynamics Starting at a Conical Intersection: Application to the Photochemistry of Pyrrole. *J. Chem. Phys.* **2009**, *131*, 024312 (1−10).

(83) Asturiol, D.; Lasorne, B.; Worth, G. A.; Robb, M. A.; Blancafort, L. Exploring the Sloped-to-Peaked S_2/S_1 Seam of Intersection of Thymine with Electronic Structure and Direct Quantum Dynamics Calculations. *Phys. Chem. Chem. Phys.* **2010**, *12*, 4949−4958.

(84) von Sonntag, C.; Schuchmann, H.-P. The Elucidation of Peroxyl Radical Reactions in Aqueous Solution with the Help of Radiation-Chemical Methods. *Angew. Chem. Int. Ed.* **1991**, *30*, 1229−1253.

(85) Calvert, J. G.; Pitts, J. N. *Photochemistry*; John Wiley: New York, 1966.

(86) Yamaji, T.; Saito, T.; Hayamizu, K.; Yanagisawa, M.; Yamamoto, O.; Wasada, N.; Someno, K.; Kinugasa, S.; Tanabe, K.; Tamura, T.; et al. *Spectral Database for Organic Compounds SDBS*; National Institute of Advanced Industrial Science and Technology (AIST): Tokyo, 2013.

(87) *Advanced Chemistry Development*, I. A. L.; 11.01 ed.

(88) Xu, H.; Wentworth, P. J.; Howell, N. W.; Joens, J. A. Temperature Dependent near-UV Molar Absorptivities of Aliphatic Aldehydes and Ketones in Aqueous Solution. *Spectrochim. Acta Part A* **1993**, *49*, 1171−1178.

(89) Mariella, R. P.; Raube, R. R. Ultraviolet Absorption Spectra of Alicyclic Compounds. II. Methyl Cycloalkyl Ketones. *J. Am. Chem. Soc.* **1952**, *74*, 518−521.

(90) Pavia, D. L.; Lampman, G. M.; Kriz, G. S.; Vyvyan, J. R. *Introduction to Spectroscopy*; Brooks/Cole Cengage Learning: Belmont, CA, USA, 2009.

(91) Glasius, M.; Lahaniati, M.; Calogirou, A.; Di Bella, D.; Jensen, N. R.; Hjorth, J.; Kotzias, D.; Larsen, B. R. Carboxylic Acids in Secondary Aerosols from Oxidation of Cyclic Monoterpenes by Ozone. *Environ. Sci. Technol.* **2000**, *34*, 1001−1010.

(92) Epstein, S. A.; Nizkorodov, S. A. A Comparison of the Chemical Sinks of Atmospheric Organics in the Gas and Aqueous Phase. *Atmos. Chem. Phys.* **2012**, *12*, 8205−8222.

(93) Epstein, S. A.; Tapavicza, E.; Furche, F.; Nizkorodov, S. A. Direct Photolysis of Carbonyl Compounds Dissolved in Cloud and Fog Droplets. *Atmos. Chem. Phys.* **2013**, *13*, 9461−9477.

(94) Seinfeld, J. H.; Pandis, S. N. *Atmospheric Chemistry and Physics - from Air Pollution to Climate Change*; John Wiley & Sons: Hoboken, NJ, USA, 2006.

(95) Hobbs, P. V. *Aerosol-Cloud-Climate Interactions*; Academic Press: London, U.K., 1993.

(96) Monod, A.; Doussin, J. F. Structure-Activity Relationship for the Estimation of OH-Oxidation Rate Constants of Aliphatic Organic Compounds in the Aqueous Phase: Alkanes, Alcohols, Organic Acids and Bases. *Atmos. Environ.* **2008**, *42*, 7611−7622.

(97) Doussin, J. F.; Monod, A. Structure-Activity Relationship for the Estimation of OH-Oxidation Rate Constants of Carbonyl Compounds in the Aqueous Phase. *Atmos. Chem. Phys. Discuss.* **2013**, *13*, 15949−15991.

(98) Kwok, E. S. C.; Atkinson, R. Estimation of Hydroxyl Radical Reaction Rate Constants for Gas-Phase Organic Compounds Using a Structure-Reactivity Relationship: An Update. *Atmos. Environ.* **1995**, *29*, 1685−1695.

(99) *NCAR Tropospheric Ultraviolet & Visible (TUV) Radiation Model*; National Center for Atmospheric Research, Atmospheric Chemistry Division: Boulder, CO, 2012; Vol. Edition 4.4.

(100) Hummel, J. R.; Reck, R. A. A Global Surface Albedo Model. *J. Appl. Meteor.* **1979**, *18*, 239−253.

(101) Rohrer, F.; Berresheim, H. Strong Correlation between Levels of Tropospheric Hydroxyl Radicals and Solar Ultraviolet Radiation. *Nature* **2006**, *442*, 184−187.

(102) Donahue, N. M.; Robinson, A. L.; Stanier, C. O.; Pandis, S. N. Coupled Partitioning, Dilution, and Chemical Aging of Semivolatile Organics. *Environ. Sci. Technol.* **2006**, *40*, 2635−2643.

(103) Pankow, J. F. An Absorption Model of the Gas/Aerosol Partitioning Involved in the Formation of Secondary Organic Aerosol. *Atmos. Environ.* **1994**, *28*, 189−193.

(104) Matsunaga, S.; Mochida, M.; Kawamura, K. Growth of Organic Aerosols by Biogenic Semi-Volatile Carbonyls in the Forestal Atmosphere. *Atmos. Environ.* **2003**, *37*, 2045−2050.

(105) Henry, K. M.; Donahue, N. M. Photochemical Aging of α-Pinene Secondary Organic Aerosol: Effects of OH Radical Sources and Photolysis. *J. Phys. Chem. A* **2012**, *116*, 5932−5940.

(106) Donahue, N. M.; Chuang, W.; Epstein, S. A.; Kroll, J. H.; Worsnop, D. R.; Robinson, A. L.; Adams, P. J.; Pandis, S. N. Why Do Organic Aerosols Exist? Understanding Aerosol Lifetimes Using the Two-Dimensional Volatility Basis Set. *Environ. Chem.* **2013**, *10*, 151−157.